이학박사 학위논문

혈청에서 바이오마커의 비표지 검출과 역전기투석 기반의 새로운 약물 전달 시스템

Label-Free Detection of Biomarkers in Human Serum and a New Drug Delivery System Based on Reverse Electrodialysis

2016년 8월

서울대학교 대학원

화학부 전기분석화학전공

권 승 용

A Ph.D. Dissertation entitled

Label-Free Detection of Biomarkers in Human Serum and a New Drug Delivery System Based on Reverse Electrodialysis

By Seung-Ryong Kwon
Major: Electroanalytical Chemistry

Submitted as partial fulfillment of the requirements for the Doctor of Philosophy degree in Chemistry

Advisor: Prof. Taek Dong Chung

Seoul National University
August 2016

Abstract

Part 1: Label-Free Detection of Biomarkers in Human Serum

A rapid and sensitive detection as well as quantification of peptides and proteins from complex biological samples is of importance for disease diagnosis. Such disease-associated macromolecules, existing in very low levels in biological samples, relate their concentration with the degree of disease progression. To monitor the level of peptides and proteins, matrix-assisted laser desorption/ionization time-of-flight mass spectrometry (MALDI-TOF MS) has been used owing to its high sensitivity (< fmol) and time-saving properties with a wide detection range of molecular mass. However, MALDI-TOF MS suffers from interferences of a variety of highly abundant peptides, proteins, salts, and other contaminants when detecting target molecules with extremely low concentration (~nM) directly from complex biosamples. As such, preseparation and enrichment of proteins are essential for the detection of these low abundant proteins prior to MS analysis.

Label-free sensing technologies provide rapid detection of multiple biomarkers in complex biosamples such as cerebrospinal fluid, urine, and blood. Nonspecific bindings are an important issue in the case of the label-free detection methodologies because any species adsorbed on the sensor surface may produce a signal, leading to the reduced accuracy and reliability of sensors. Thus, identification of the degree of disease progression and diagnosis become difficult. In this study, we functionalized Au-plated magnetic microspheres (MGMs) with self-assembled monolayers (SAMs) for the effective prevention of the nonspecific bindings in human serum. The SAM employed in this study was composed of a chain of oligo ethylene glycol for preventing non-specific bindings and terminal carboxyl group for antibody immobilization. The antibody-conjugated MGMs were exposed to human serum to enrich target antigens specifically and the antigen-conjugated MGMs were directly analyzed by MALDI-TOF MS. To investigate the degree of nonspecific bindings and target enrichment, we compared the MGMs with four types of commercial magnetic microbeads. As the results, the MGMs showed superior enrichment properties out of the beads

tested while providing effective suppression of the nonspecific bindings. Especially, the detection limit of myoglobin was 0.5 ng/mL in human serum using the MGMs. Finally, we conducted multiple detection of biomarkers in human serum simultaneously by taking both advantages of MALDI-TOF MS (label-free detection) and the MGMs (suppression of nonspecific bindings).

Part 2: A New Drug Delivery System Based on Reverse Electrodialysis

Recently, reverse electrodialysis (RED) has been attracted great attention of scientists as an alternative way of power production due to use of inexhaustible resources (seawater and river water) and stable power production. However, there are still obstacles in scale-up applications, for example, high cost and short lifetime of ion-exchange membranes and low power density compared with the current power production methods. In this study, we developed a new transdermal drug delivery system based on RED as an electrical power source. For the purpose of power production in a large scale, RED system requires electrodes at the ends of the cell to relay the

generated power to an external circuit. However, a miniaturized RED patch for transdermal drug delivery does not involve any metal electrodes to introduce the electrical power into a biological system because both systems comprise only ionic current. Thus, the patch-type RED system that generates a low power can be suitably utilized for the purpose of transdermal drug delivery. The penetration rate of risedronate (RIS) was 36-fold higher with the RED patch than with a diffusive patch. We finally conducted *in vivo* experiments using osteoporosis-induced female mice by removing the ovary. As the results, the mice treated with RIS by means of the RED patch were effectively prevented from proceeding osteoporosis while the mice treated with RIS only by passive diffusion led to very similar results to the ovary-removed mice, showing almost no therapeutic effects.

Keywords: magnetic gold microspheres, nonspecific binding, mass spectrometry, reverse electrodialysis, transdermal drug delivery, osteoporosis

Student Number : 2011-30098

Table of Contents

List of Figures

List of Tables

1. Gold-Plated Magnetic Polymers for Highly Specific Enrichment and Label-Free Detection of Blood Biomarkers in Human Serum

1.1 Introduction

A rapid, sensitive detection and quantification of biomarkers in complex physiological samples are of importance for disease diagnosis. [1-3] Such disease-associated macromolecules, existing in very low levels in blood, continue to be discovered and relate their *in situ* concentrations to the degree of disease progression. [4-7] Thus, multiplex detection of biomarkers becomes prerequisite, which would be ideally complemented by label-free sensing technologies, such as suspension arrays [8-10] and MALDI-TOF MS. [3,11-14] While the high sensitivity and broad detection range of MALDI-TOF MS have spurred proteomics research, detection of specific biomolecules requires efficient enrichment using affinity probe-conjugated nanoparticles [11,12,15-18] or magnetic microspheres. [19-23] Especially, microspheres, coupled with the advances in flow

cytometry technologies, have improved clinical diagnoses by allowing high throughput screening of drugs, genes, and proteins. [24,25] Despite their great potential, mutually exclusive obstacles such as dilution factors and matrix effects continue to limit the assay performance; an inappropriate diluent and dilution factor may lead to a clinically irrelevant result, [26] while real-life physiological matrices (blood, serum, or pleural effusion) induce heavy nonspecific binding to the solid supports. [11,25,27] Such unwanted biofouling inevitably masks sensor surfaces, reducing not only the specificity and sensitivity but the accuracy of quantification. [14,28-31] In cases of label-free assays, nonspecific binding brings more negative repercussions because any biomolecule that binds to the sensor will produce signal. [3] In an effort to address the issue, Davis and coworkers employed PEG-thiol self-assembled monolayers (SAMs) [32,33] and zwitter ionic poly-carboxybetaine methacrylate (pCBMA) [34] on Au electrodes for an electrochemical detection of a single protein biomarker in neat blood serum. The results imply that high density of hydrophilic and charged moiety is required for the efficient protection of biofouling. Previously, we showed that polymer

beads, when protected with thin gold layers and PEG SAMs, exerted superior enrichment and isolation of the target molecules in intact serum, while bare polymer beads could not. [35] Herein, on the basis of previous results, we systematically compare the nonspecific binding of serum proteins and the enrichment capability between the Au-plated magnetic microspheres (MGMs) and the other microspheres, and thereby propose an extended applicability of the MGMs to a label-free detection of multiple biomarkers using MALDI-TOF MS (**Fig. 1-1**).

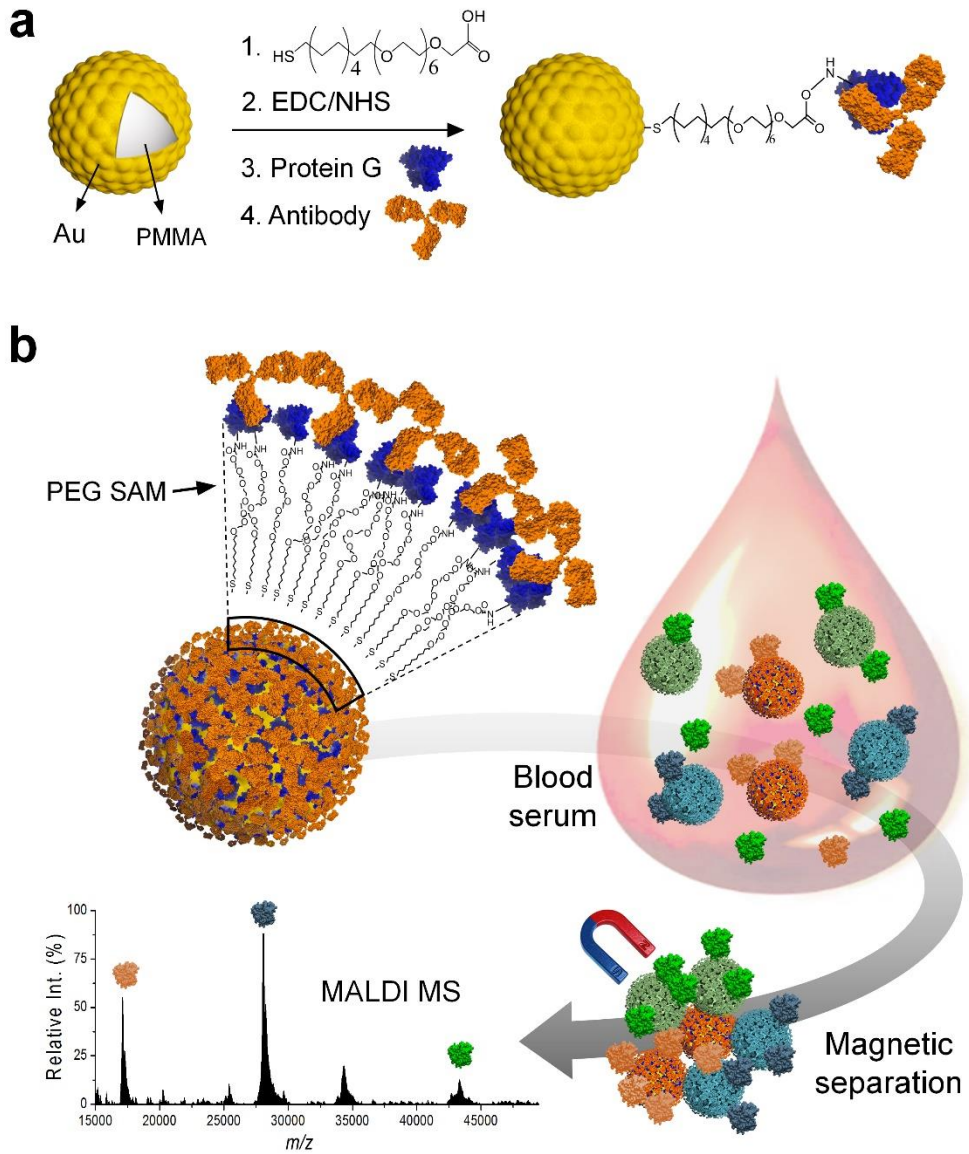

Fig. 1-1 Schematic illustration of manufacturing the affinity probe-conjugated magnetic gold microspheres (MGMs) (a) and their applications to the enrichment of target proteins in human serum for multiplexed label-free mass analysis (b).

1.2. Experimental Section

1.2.1. Materials

Cytochrome C (C2037), sinapinic acid (85429), 1-ethyl-3-(3-dimethylaminopropyl)-1-carbodiimide hydrochloride (EDC), *N*-hydroxysuccinimide (NHS), human serum (AB type), prostate specific antigen (PSA, P3235) and protein G recombinant (19459) were purchased from Sigma-Aldrich (St. Louis, MO). Carboxyl-terminated hexa(ethylene glycol) undecane thiol (CMT002) was obtained from Nanoscience Instruments (Phoenix, AZ). Myoglobin, creatine kinase-muscle brane (CK-MB, 30-AC65), rabbit polyclonal anti-myoglobin antibody (70-MR13), and myoglobin-free human serum (90R-110) were from Fitzgerald (North Acton, MA). Mouse monoclonal anti-PSA antibody (ab403, isotype: IgG1) and mouse monoclonal anti-CK-MB antibody (ab19603, isotype: IgG1) were obtained from Abcam (Cambridge, UK). Magnetic gold microspheres (MGMs) (M-NG0501, 15 μm in diameter, Nomadien.com) were constructed using proprietary methods including electroless plating of auric acids on proprietary magnetic poly(methylmethacrylate) (PMMA) beads (Nomadien.com). 15 μm

carboxyl-functionalized polymer beads (PC07N) and 7.9 μm carboxyl-functionalized magnetic beads (UMC4N) were from Bangs Laboratories (Fishers, IN). 2.8 μm protein G-conjugated magnetic beads (Dynabeads, 10003D) were purchased from Life technologies (Carlsbad, CA). 2 μm protein G-conjugated magnetic beads (S1430S) were obtained from New England Biolabs (Ipswich, MA). PBS buffer solution (pH 7.4) was composed of 0.01 M phosphate buffered saline, 0.138 M NaCl, and 0.0027 M KCl. TTBS buffer solution (pH 7.4) was composed of 0.05% (v/v) Tween-20, 20 mM Tris-HCl and 150 mM NaCl.

1.2.2. Antibody conjugation of MGMs with orientation control

MGMs (0.63 mg) and absolute ethanol (0.5 mL) were added into a centrifuge tube and sonicated for a few seconds for dispersion. Then, MGMs were collected in the tube by a magnetic force while removing ethanol solution. MGMs were suspended in 0.5 mL of ethanolic solution containing 1 mM carboxyl-terminated alkanethiol to generate self-assembled monolayers (SAMs) for about 1 week at room temperature (RT) with gentle rotation. After the formation of

SAMs, MGMs were washed with distilled water several times by collecting MGMs with a magnetic force, pipetting off the unwanted solutions, and refilling distilled water into the tube respectively. EDC (2 mM) and NHS (5 mM) in 0.5 mL of MES (50 mM, pH 5.5) were added into MGMs to activate carboxyl groups for coupling with protein G. The solution was then incubated with gentle shaking for 30 min at RT and removed by magnetic separation. Protein G (10.5 μg in 85 μL MES) was allowed to bind covalently with the SAM-protected MGMs for 12 h at RT and washed with PBS (10 mM, pH 7.4) three times. Addition of IgG proteins (10.5 μg in 105 μL PBS) into the protein G-modified MGMs were followed and incubated for 2 h at RT. The antibody-conjugated MGMs were washed with PBS three times to achieve the complete removal of unbound excess antibodies. The resulting products were dispersed in a PBS solution and stored at 4 °C.

1.2.3. Antibody conjugation of MGMs without orientation control

SAM-protected MGMs (0.48 mg) was reacted with 2 mM EDC/5mM NHS in 0.5 mL MES buffer solution for 30 min at RT. The

MGMs were magnetically collected while removing the supernatant. Then IgG proteins (4 μg in 40 μL of MES buffer solution) were immediately added into the centrifuge tube containing the MGMs for the conjugation of the IgG proteins to the MGMs via covalent bonds for overnight at RT. The antibody−conjugated MGMs were washed with PBS three times to achieve complete removal of unbound excess antibodies. The resulting products were dispersed in a PBS solution and stored at 4 °C.

1.2.4. Quantification of surface carboxy groups on microspheres

We followed a simple colorimetric method developed by Andreas Henning et al. [45] Briefly, varying amounts of microsphere were incubated with 200 μM Ni^{2+} for 2 min in 10 mM HEPES buffer, pH 7.5 (total volume 0.6 mL). The solution was centrifuged at 16000 rcf for 1 min. 500 μL of the supernatant of the solution was diluted with 490 μL of HEPES buffer and then 10 μL of pyrocatechol violet (PV) was added (40 μM in the final volume 1 mL). The absorbance at 650 nm was plotted with respect to the amounts of microsphere stock solution. Linear fitting of the initial decrease gave the slope a and

the y−intercept b. The number of surface carboxy groups obtained by the following equation

$$\text{surface carboxy groups}\left(\frac{\mu\text{mol}}{\text{particle}}\right)=\frac{n[\mathrm{M}^{2+}]Va}{w(A_{\mathrm{PV}}-b)}$$

where V is the volume and $[\mathrm{M}^{2+}]$ the metal ion concentration, a the slope, b the y−intercept of the initial linear decrease, A_{PV} the absorbance of PV in the absence of M^{2+}, w the particle concentration (in particles mL^{-1}) of the stock solution, and n, 2.65, a stoichiometry factor indicating the number of surface carboxy groups per metal cation.

1.2.5. Immunoassays in human serum using antibody−modified MGMs

Antibody−conjugated MGMs (60 μg, ~49500 beads) were suspended in a 0.5 mL human serum containing a desired concentration of antigen and incubated for 30 min with gentle rotation at RT. Then, antigen−captured MGMs were washed with TTBS and water for 2 times respectively. Antigen−captured MGMs were mixed with 1.2 μL of matrix solution (7.5–15 mg mL^{-1} sinapinic acid in

50:50:0.1 (v/v/v) acetonitrile, water, trifluoroacetic acid containing 5–10 fmol μL^{-1} cytochrome C as internal standard) and the mixture solution with all antigen-captured MGMs was pipetted onto the sample plate directly for MALDI-TOF MS analysis. Notably, myoglobin quantification was conducted using orientation-controlled antibody-conjugated MGMs via protein G affinity. Quantification of PSA and CK-MB were conducted using random-oriented antibody-conjugated MGMs.

1.2.6. Kinetic study of immunoreactions of antibody-conjugated MGMs and antigens

Antibody-conjugated MGMs (70 μg) were dispersed in 0.7 mL of sample solution (0.5 μg mL^{-1} Myo, 10 mM PBS, pH 7.4) with gentle rotation and allowed for immunoreactions at RT. At a desired time (3, 7, 12, 20, 30, and 60 min), 0.1 mL of sample solution containing the antigen-captured MGMs (10 μg) was transferred to a new centrifuge tube and immediately washed with PBS and water for two times each to stop further immunoreactions. Then, the antigen-captured MGMs were analyzed by MALDI-TOF MS.

1.2.7. Comparison of the MGMs modified with orientation-controlled antibodies with commercial beads

Carboxyl-functionalized magnetic (7.9 μm in diameter) and non-magnetic (15 μm in diameter) beads (Bangs Lab), protein G-modified magnetic beads (2 μm in diameter, New England BioLabs), and protein G-modified magnetic Dynabeads (2.8 μm in diameter, Life Technologies) were functionalized with Myo antibodies by following the exactly same procedures for the preparation of Myo antibody-conjugated MGMs (15 μg, ~12400 beads). All microspheres were reacted with 0.2 mL of human serum spiked with Myo (0.2 μg) for 30 min at RT. The reacted beads were washed with TTBS and water for two times, then analyzed by MALDI-TOF MS.

1.2.8. Comparison of the MGMs with random-oriented antibodies with commercial beads

Carboxyl-functionalized magnetic beads (7.9 μm in diameter, 178000 beads; 15 μm, 49500 beads, Bangs Lab) were functionalized with PSA antibodies by following the same procedures for the

preparation of PSA antibody-conjugated MGMs (60 μg, ~49500 beads). All microspheres were immunoreacted with 0.5 mL human serum spiked with 5 ng PSA for 1 h at room temperature. The reacted beads were washed with TTBS and water for two times, then analyzed by MALDI-TOF MS.

1.2.9. Multiplex immunoassay

Each of Myoglobin, CK-MB, and PSA antibodies was conjugated to SAM-protected MGMs (15 μg) in a random orientation manner. Three types of antibody-conjugated MGMs (45 μg) were immunoreacted with a 0.5 mL human serum spiked with 25 ng Myo, 50 ng CK-MB, and 50 ng PSA for 30 min at RT. The antigen-captured MGMs were washed with TTBS and water for two times then applied to MALDI-TOF MS analysis.

1.2.10. MALDI-TOF mass spectrometry

Matrix solution (1.2 μL of 7.5–15 mg mL^{-1} sinapinic acid in 50:50:0.1 (v/v/v) acetonitrile, water, trifluoroacetic acid) was used to assist protein desorption and ionization from the bead surface. The

mixture solution composed of the matrix solution and target-captured beads was pipetted onto the sample plate directly for MALDI-TOF MS analysis. Mass analysis was carried out using a Voyager DE^{TM} Biospectrometry mass spectrometer (Applied Biosystems) with 337-nm nitrogen laser at the Seoul National University National Center for Inter-University Research Facilities (NCIRF). Typical experimental parameters were as follows: Linear mode of operation, positive polarity, 25000 VDC accelerating voltage, 92% grid voltage, 500-ns delayed extraction, and 2 kDa of low mass gate. For the quantifications of Myo, CK-MB and PSA in human sera, we used fixed laser intensity and repetition frequency (1455 and 20.0 Hz). Spectra were obtained by averaging ~400 shots followed by a Gaussian smoothing and baseline correction (optional) using Data-Explorer software (Applied Biosystems).

1.2.11. Field-Emission Scanning Electron Microscopy (FE-SEM)

The surface morphology of MGMs on a carbon tape was monitored using JSM 5410LV (JEOL, Japan) with 2 kV of acceleration voltage at the National Instrumentation Center for Environmental

Management (NICEM) of Seoul National University.

1.3. Results and Discussion

To investigate the degree of nonspecific bindings and target enrichment, we chose myoglobin (Myo), a 17 kDa biomarker for cardiovascular disease (CVD) as a model target. Myo exists at tens of ng mL^{-1} in normal human sera, whereas during acute myocardial infarction its population increases within three hours. [36,37] We compared MGMs with four types of microspheres that are broadly used for diagnostics and bioseparations: carboxyl-functionalized magnetic polymer beads (7.9 μm in diameter, Bangs Lab) carboxyl-functionalized polymer beads (15 μm in diameter, Bangs Lab), and protein G-conjugated magnetic beads with the diameter of 2 μm (New England Biolabs) and 2.8 μm (Dynabeads, Life Technologies). We initially generated SAMs on MGMs using carboxyl-terminated hexa(ethylene glycol) undecane thiol. [35] After the SAM formation, recombinant protein G was conjugated with the carboxyl group of the SAM molecule using 1-ethyl-3-(3-dimethylaminopropyl)-1-carbodiimide hydrochloride (EDC) and *N*-hydroxysuccinimide (NHS). [38] Likewise, the carboxyl-functionalized polymer microspheres were directly modified with protein G using EDC/NHS

chemistry. Myo antibodies were then immobilized via protein G–Fc heavy chain interactions, rendering both antigen binding Fab chains optimally exposed to the assay media. Such oriented antibodies usually increase total antigen binding activity as compared to that of randomly oriented antibodies. [39–41] For MGMs, each modification step, magnetic properties, and the capability of Myo enrichment from PBS solution were verified using MALDI MS (**Fig. 1–2, 1–3, and 1–4**).

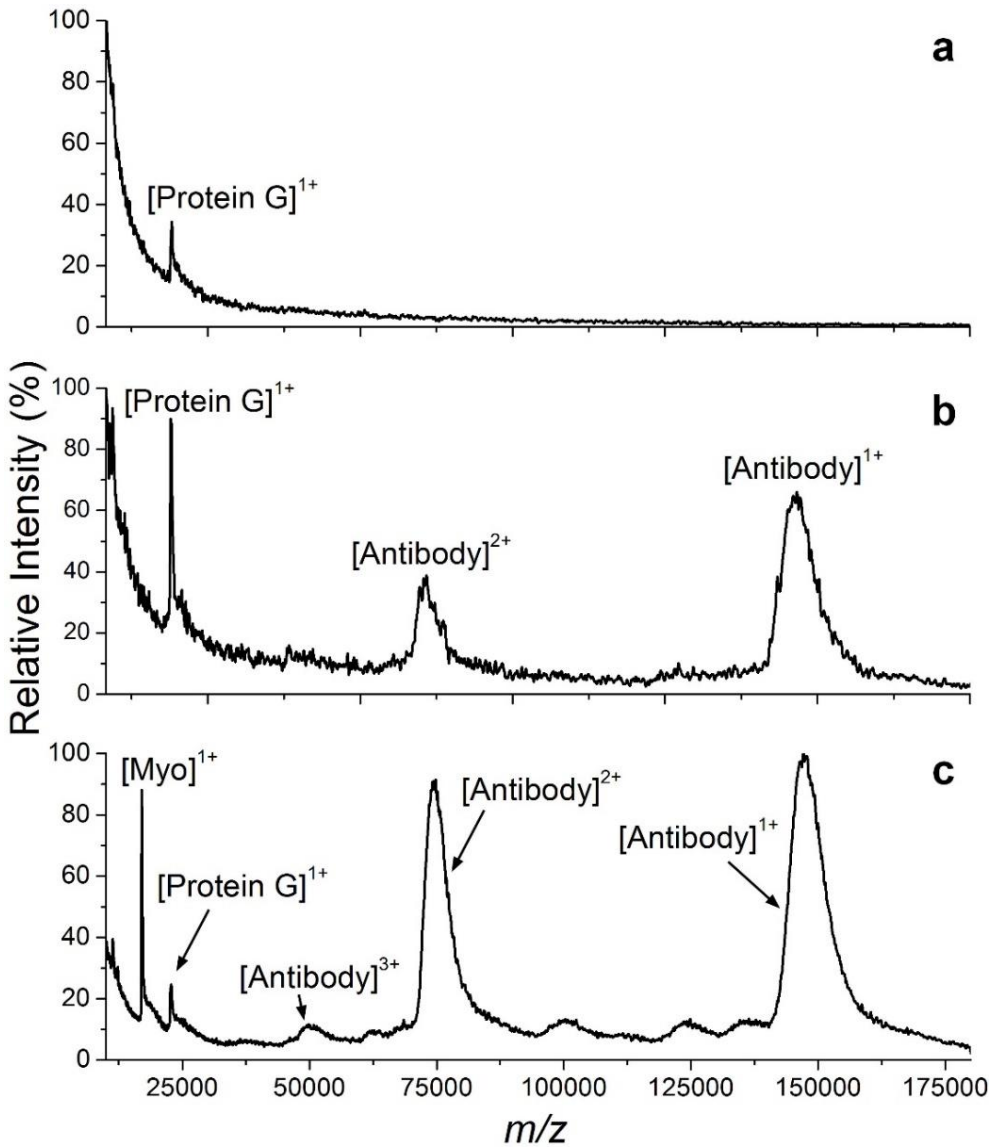

Fig. 1-2. MALDI-TOF mass spectra of MGMs modified with protein G (a), antibody (b), and Myo enriched from a PBS solution (c).

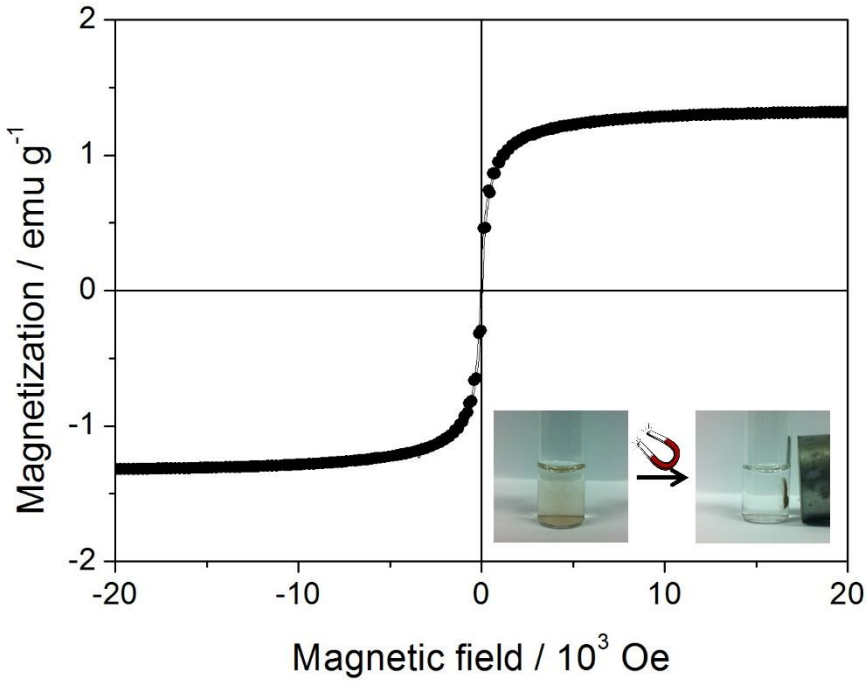

Fig. 1-3. The hysteresis loop of gold-plated magnetic microspheres after antibody immobilization.

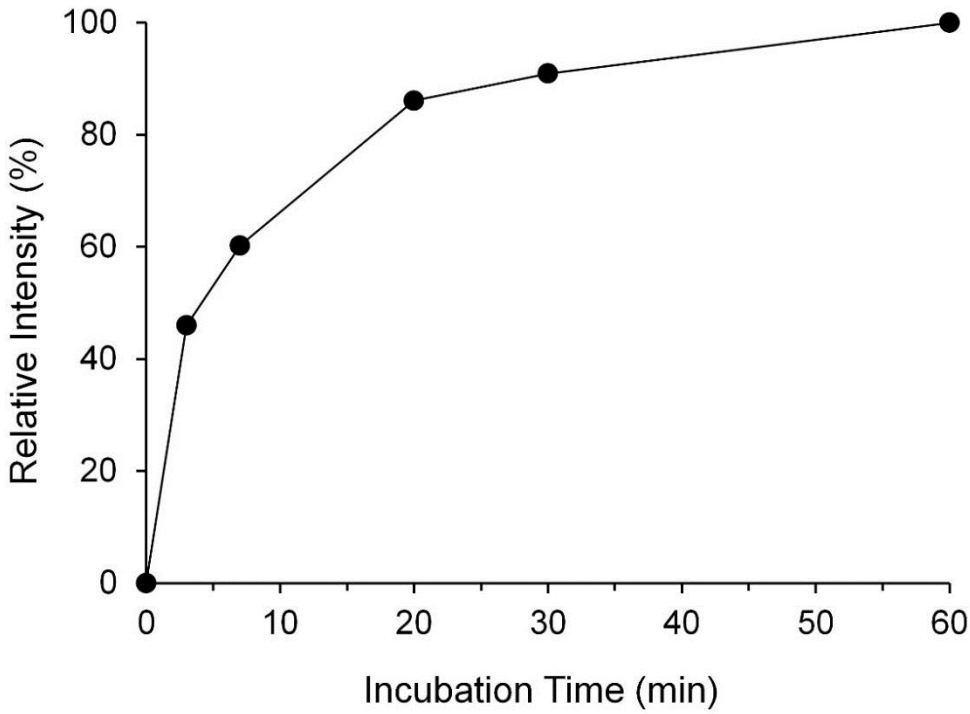

Fig. 1-4. Effect of incubation time on antibody-antigen immunoreaction using antibody-conjugated MGMs. After incubation (3, 7, 12, 20, 30, and 60 min) of Myo antibody-conjugated MGMs in the PBS solution composed of 500 ng/mL Myo, the quantities of the Myo extracted by antibody-conjugated MGMs were detected by MALDI-TOF MS. The relative peak intensity generated using the ratio of the ion intensity of Myo to the ion intensity of CytC was plotted as a function of incubation time.

We used ~12400 MGMs for the adsorption assays because the number of MGMs for adequate MALDI assays ranges from ~8200 (10 μg) to ~49500 (60 μg) for 0.5 mL serum samples (data not shown). The amount of antibodies immobilized on ~12400 MGMs was ~30 ng, lower than theoretical amount (**Fig. 1-5 and 1-6**). For comparison, we used the same number (~12,400) of 15 μm polymer beads for the surface functionalization. The number of 7.9 μm magnetic beads was adjusted to ~44600 so that the surface area of the beads matches to the one of the MGMs. In the case of commercial protein G magnetic beads (2 and 2.8 μm), the amount of microspheres was set to capture ~30 ng of antibodies according to the manufacturers' protocols. Following SDS-PAGE analysis revealed that the commercial microspheres hold greater amount of antibody than the MGMs do except the 15 μm polymer beads (**Fig. 1-7 and 1-8**). When we conducted enrichment assays using the antibody-loaded microspheres, all commercial beads, except the 15 μm polymer beads, successfully yielded Myo peaks in MALDI spectra (**from Fig. 1-9 to Fig. 1-16**). Importantly, nonspecific peaks corresponding to human serum albumin (HSA) always appeared in all

the cases of commercial beads. In contrast, the MGMs barely yielded such nonspecific peaks except an additional peak corresponding to protein G at 23 kDa due to desorption of the SAM molecules. [42]

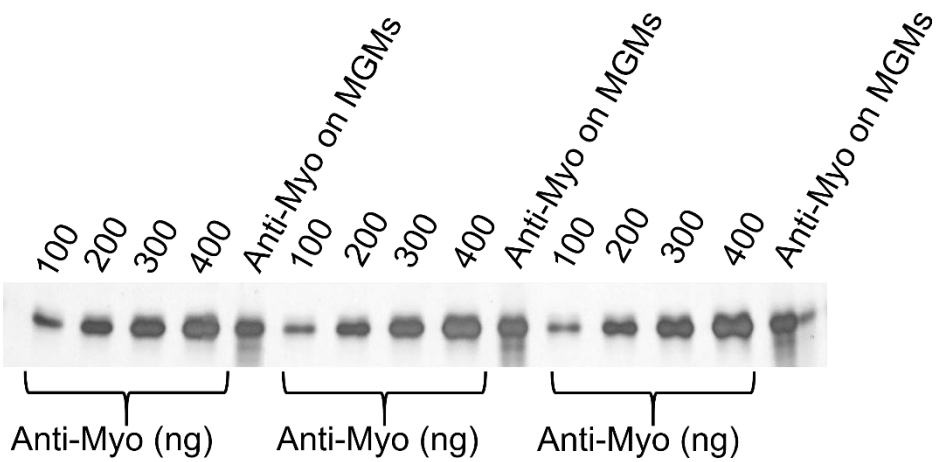

Fig. 1-5. Quantification of antibodies immobilized on MGMs. A silver-stained gel image after SDS-PAGE showing 50 kDa heavy chains of IgG.

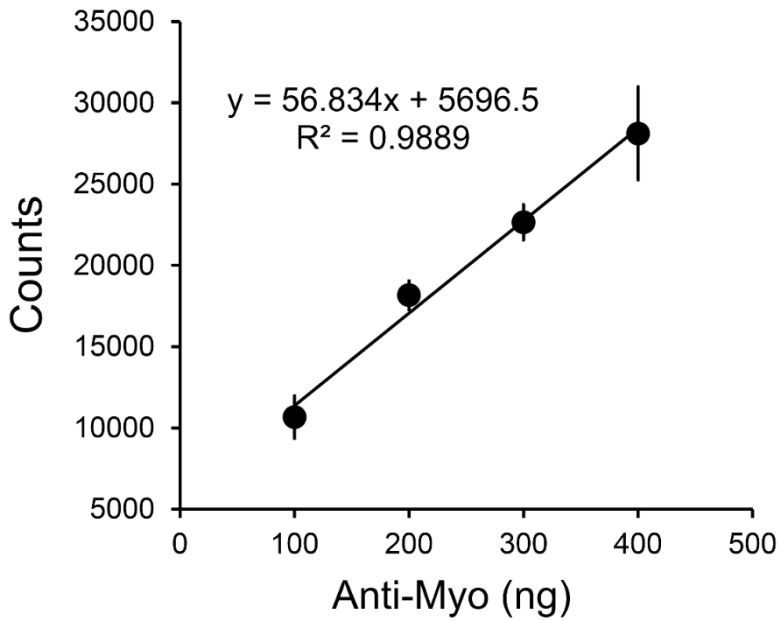

Fig. 1−6. Calibration plot calculated from the density of protein bands and the error bars represent the standard deviations of three independent measurements.

In theory, the surface area of the ~12400 MGMs is 8.77×10^{-6} m^2. If all the antibodies (spheroid shape with the dimensions of 15 nm × 15 nm × 3 nm) are packed in upright position, the maximum amount per ~12400 MGMs would be 57 ng (See *Principles in Adsorption to Polystyrene*, Peter Esser, M.Sc., Thermo Fisher Scientific Bulletin No. 6a. 2010).

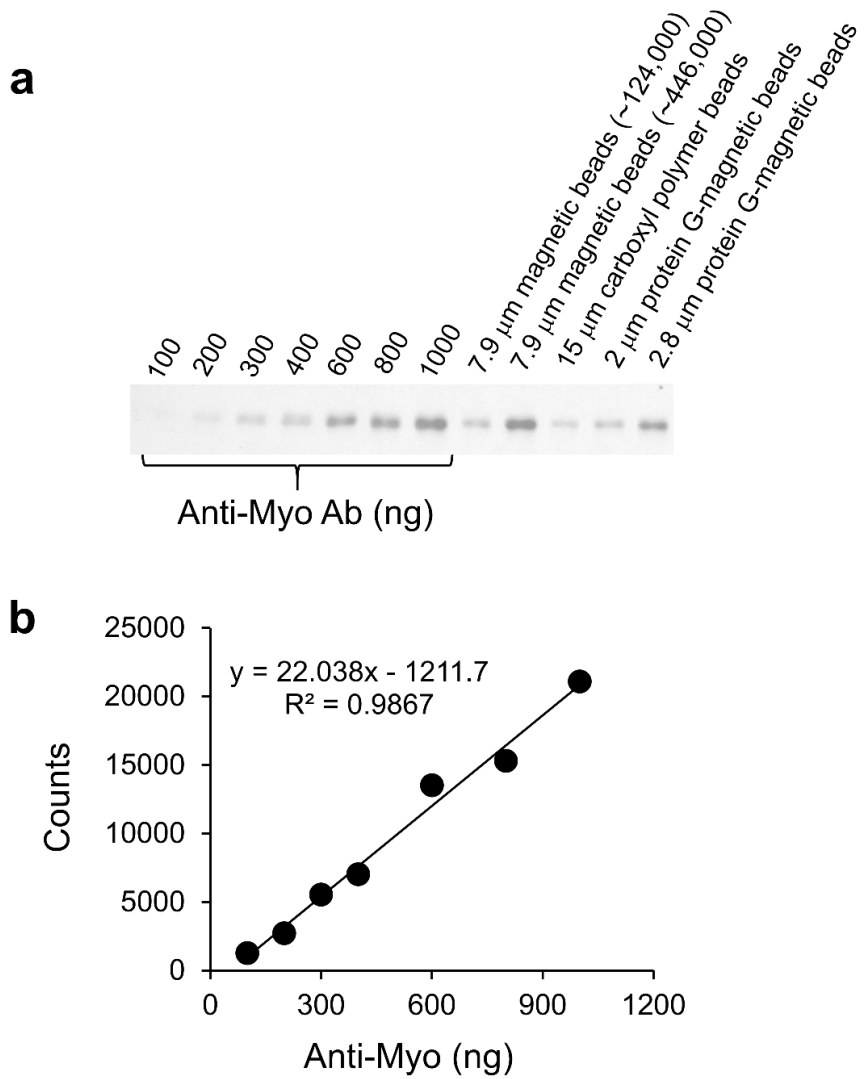

Fig. 1-7. Quantification of antibodies immobilized on the testing beads. a) A silver-stained gel image after SDS-PAGE showing 50 kDa heavy chains of IgG. b) The calibration plot obtained from the pixel density of the IgG bands using Image J software

Bead type (number used)	Antibody (ng)
15 μm MGMs (~12,400)	31
7.9 μm carboxyl-terminal magnetic (~12,400)	33
7.9 μm carboxyl-terminal magnetic beads (~44,600)	95
15 μm carboxyl-terminal polymer beads (~12,400)	22
2 μm protein G magnetic beads (NEB)	33
2.8 μm protein G magnetic beads (Dynabeads)	68

Fig. 1-8. The amount of antibodies immobilized on each microbeads is tabulated.

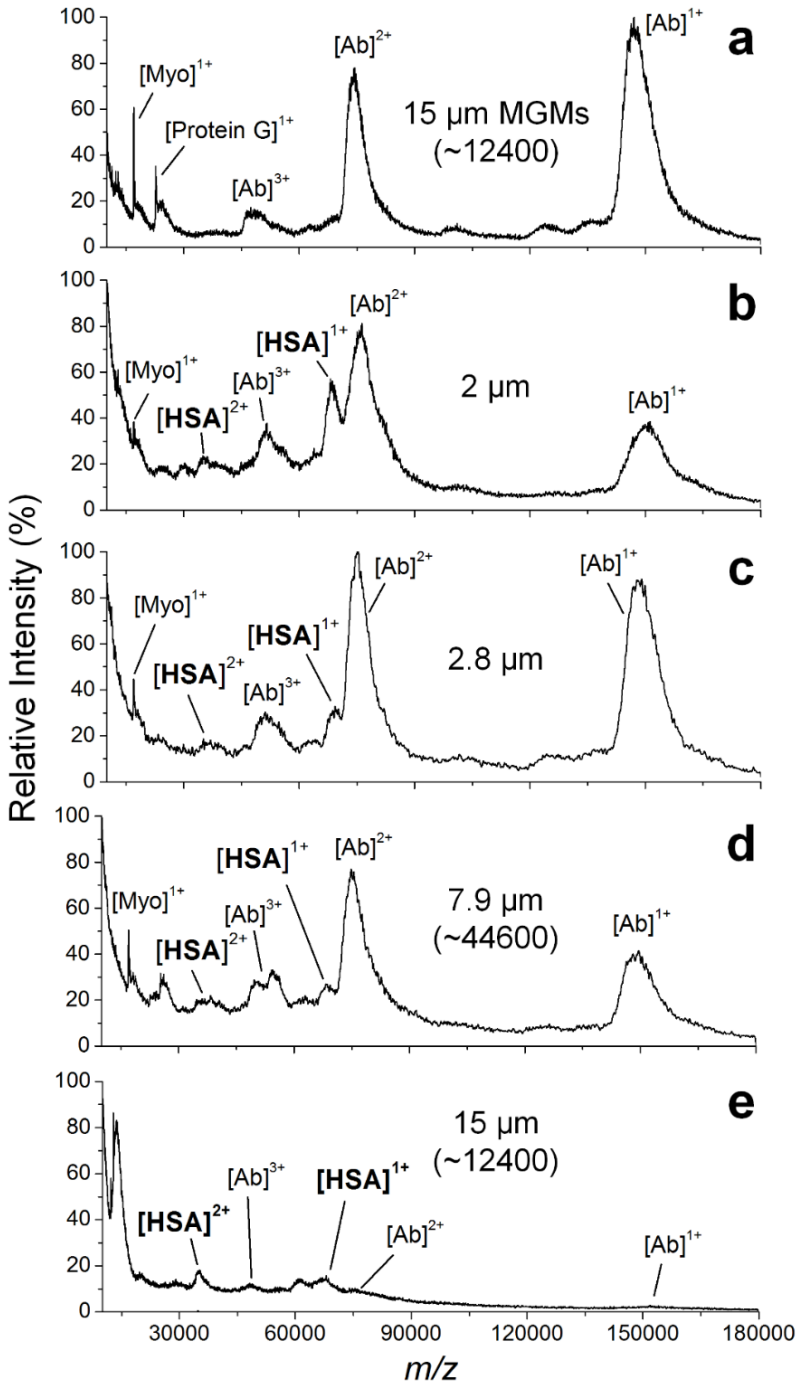
a
15 μm MGMs
(~12400)
[Myo]1+
[Protein G]1+
[Ab]3+
[Ab]2+
[Ab]1+
b
2 μm
[Myo]1+
[HSA]2+
[Ab]3+
[HSA]1+
[Ab]2+
[Ab]1+
c
2.8 μm
[Myo]1+
[HSA]2+
[Ab]3+
[HSA]1+
[Ab]2+
[Ab]1+
d
7.9 μm
(~44600)
[Myo]1+
[HSA]2+
[Ab]3+
[HSA]1+
[Ab]2+
[Ab]1+
e
15 μm
(~12400)
[HSA]2+
[Ab]3+
[HSA]1+
[Ab]2+
[Ab]1+
Relative Intensity (%)
m/z
0
20
40
60
80
100
30000
60000
90000
120000
150000
180000

Fig. 1-9. a-e) Evaluation of nonspecific adsorption and detection of Myo using MGMs in comparison with other microbeads. Representative MALDI-TOF mass spectra of microbeads after incubation with 0.2 mL of human serum spiked with 0.2 μg of Myo. a) MGMs (~12400 beads, 15 μm), b) protein G magnetic beads (2 μm; NEB), c) protein G magnetic beads (2.8 μm; Dynabeads), d) magnetic carboxyl beads (~44600 beads, 7.9 μm; Bangs Laboratories), and e) carboxyl beads (~12400 beads, 15 μm; Bangs Laboratories). Ab, antibody; HSA, human serum albumin.

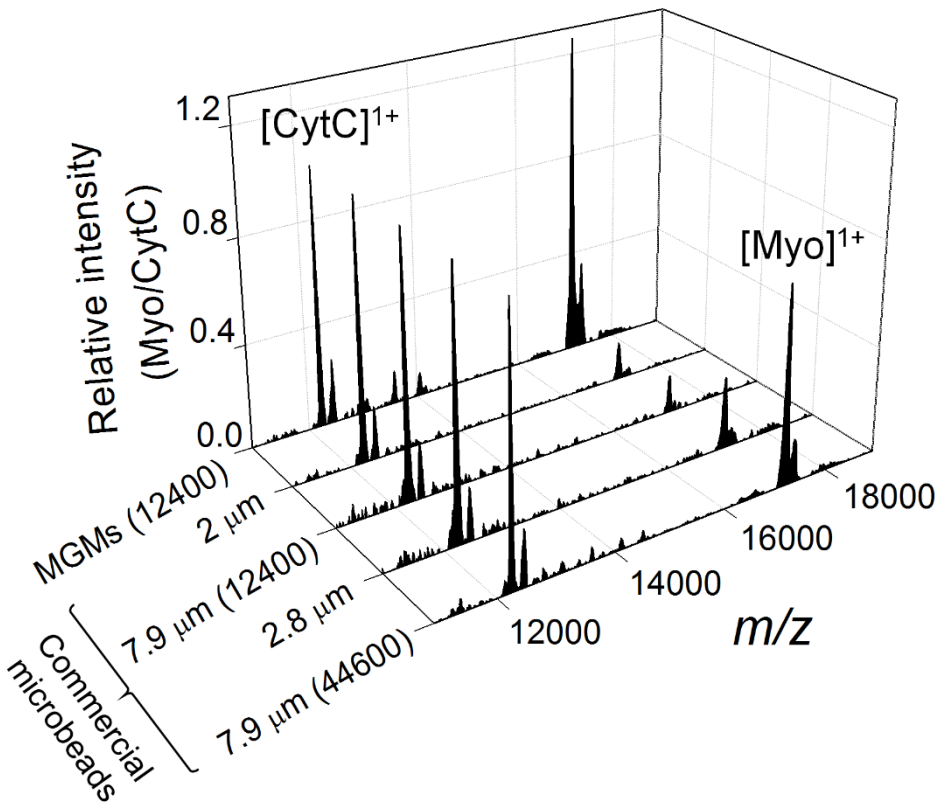

Fig. 1-10. Representative MALDI-TOF mass spectra for the affinity extraction and detection of Myo using MGMs and other microbeads. Cytochrome C (CytC) served as an internal standard.

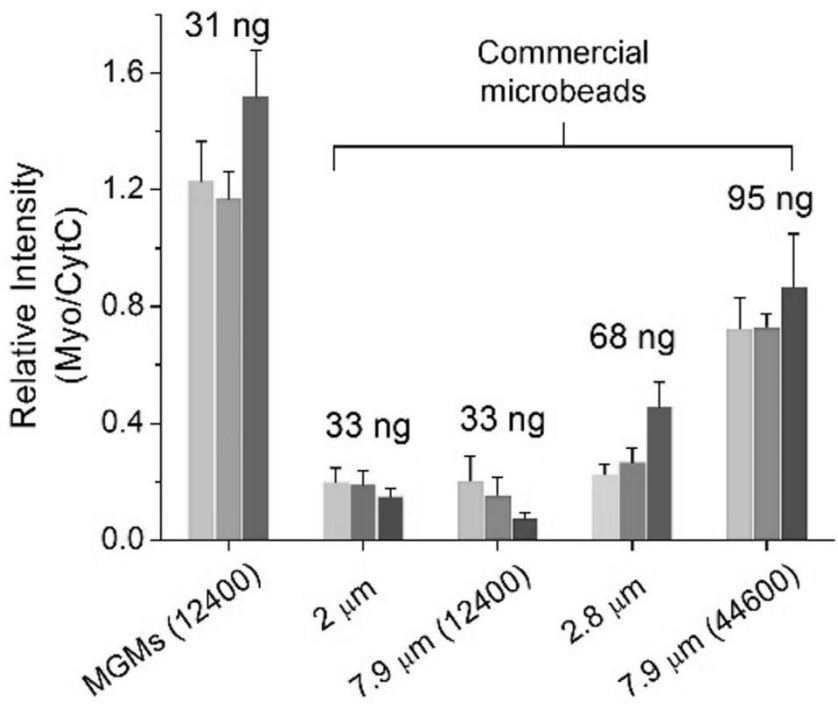

Fig. 1-11. Comparison of three sets of independent experiments. The amount of antibody immobilized on microbeads was annotated in nanograms. The error bars represent the standard deviations obtained from four to six spectra.

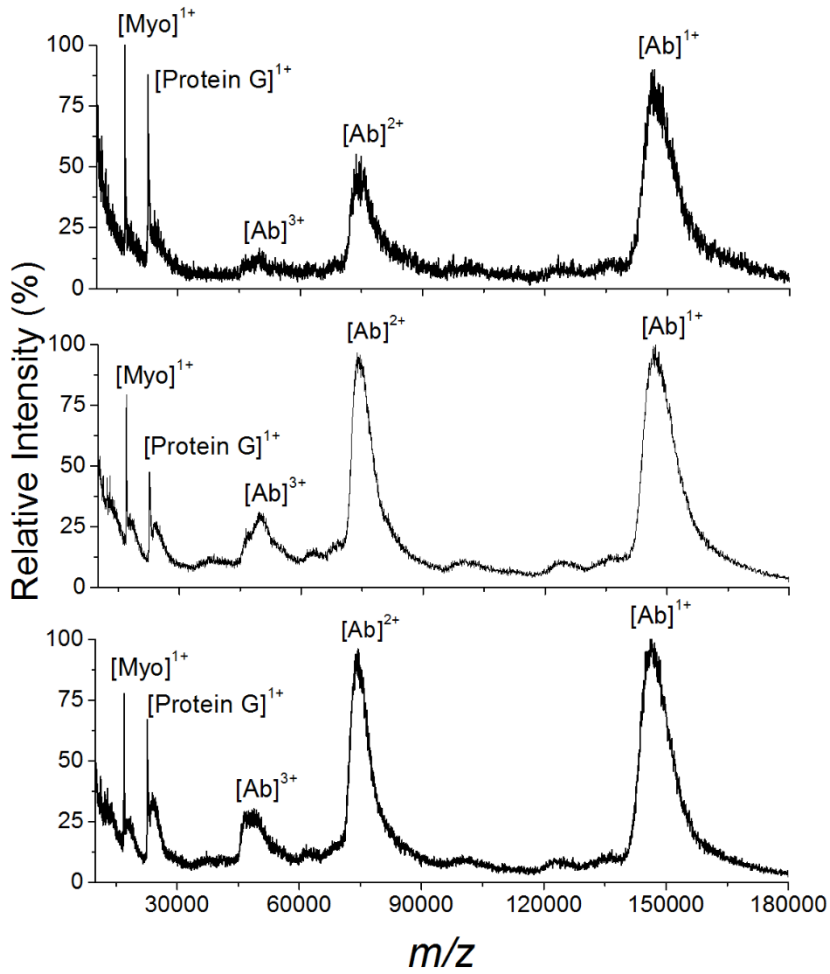

Fig. 1-12. Additional representative MALDI-TOF mass spectra of MGMs (~12400 beads, 15 μm) after incubation with 0.2 mL of human serum spiked with 0.2 μg of Myo. Spectra were obtained through two days of independent experiments. Ab, antibody; HSA, human serum albumin.

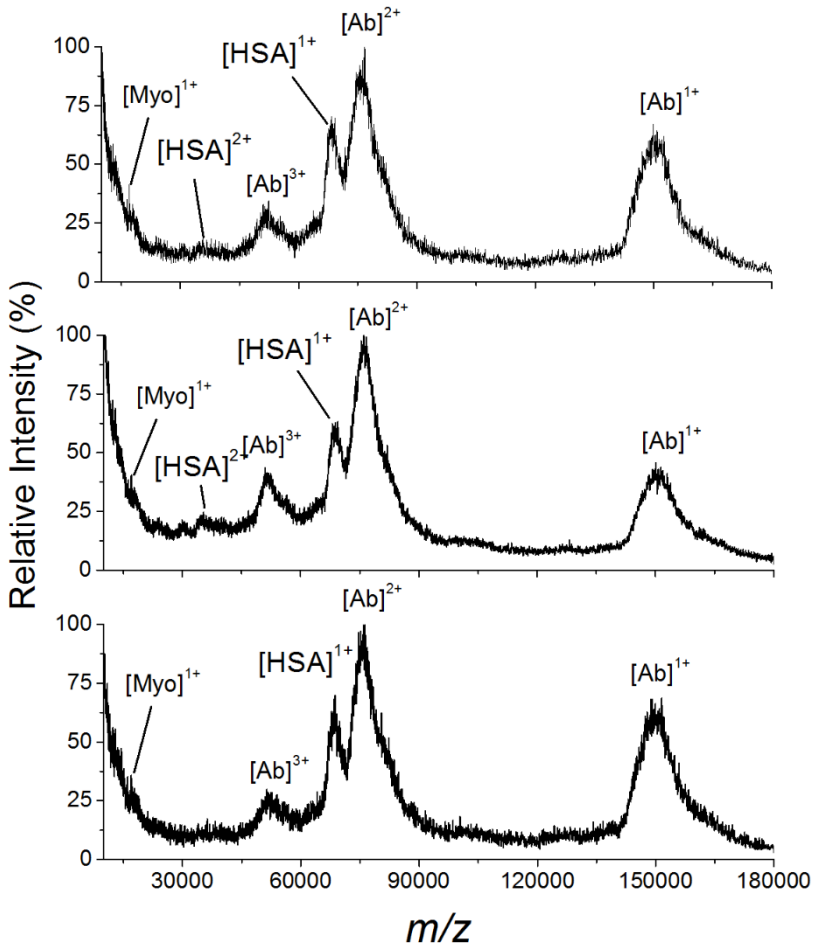

Fig. 1-13. Additional representative MALDI-TOF mass spectra of protein G magnetic beads (2 μm) after incubation with 0.2 mL of human serum spiked with 0.2 μg of Myo. Spectra were obtained through two days of independent experiments. Ab, antibody; HSA, human serum albumin.

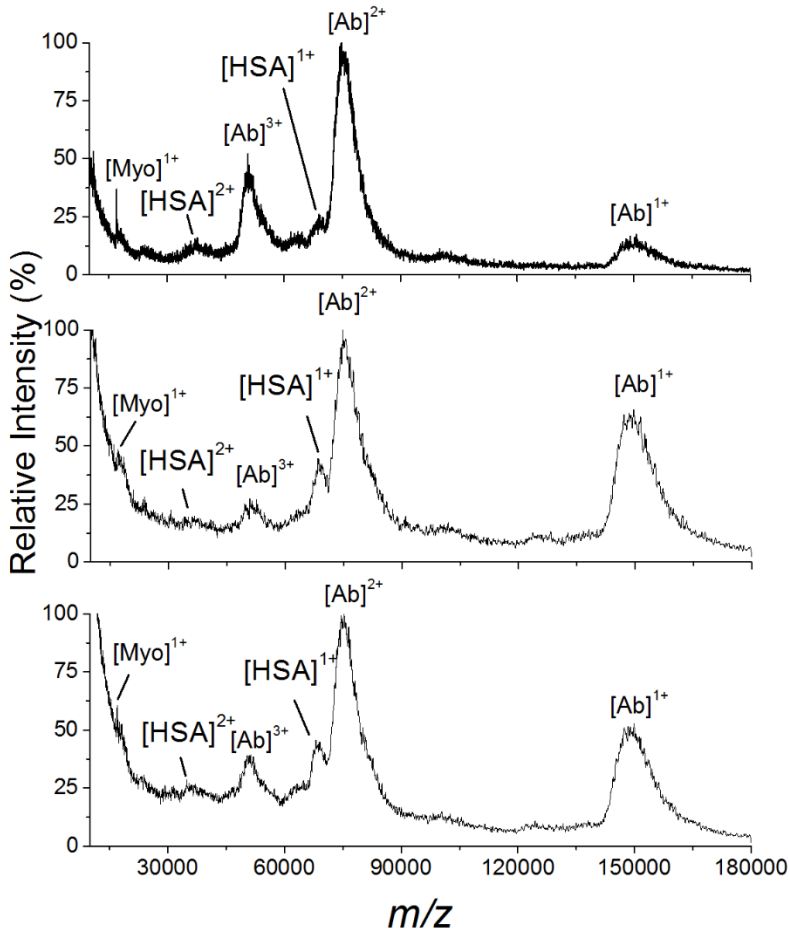

Fig. 1-14. Additional representative MALDI-TOF mass spectra of protein G magnetic beads (2.8 μm) after incubation with 0.2 mL of human serum spiked with 0.2 μg of Myo. Spectra were obtained through two days of independent experiments. Ab, antibody; HSA, human serum albumin.

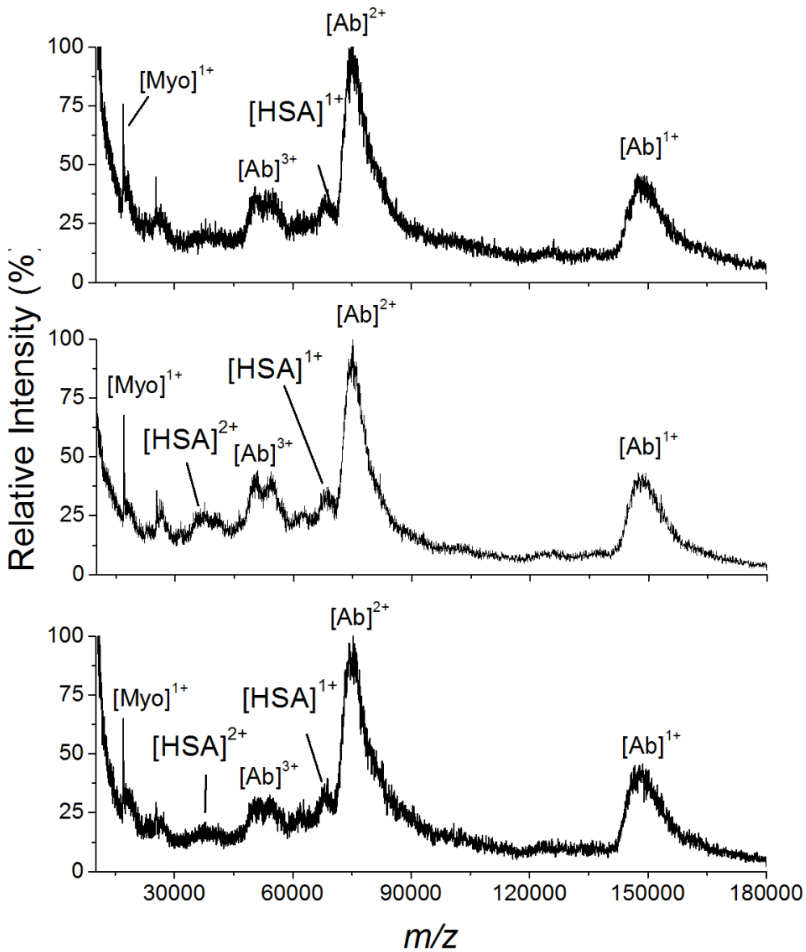

Fig. 1-15. Additional representative MALDI-TOF mass spectra of magnetic carboxyl beads (~44600 beads, 7.9 μm) after incubation with 0.2 mL of human serum spiked with 0.2 μg of Myo. Spectra were obtained through two days of independent experiments. Ab, antibody; HSA, human serum albumin.

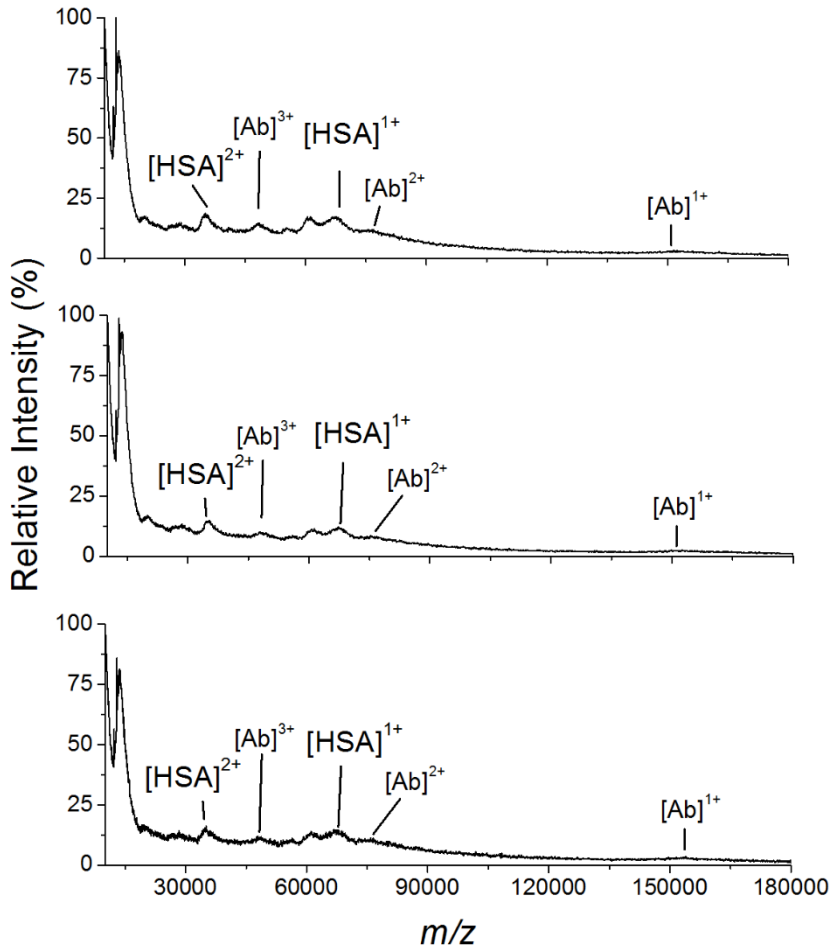

Fig. 1-16. Additional representative MALDI-TOF mass spectra of carboxyl beads (~12400 beads, 15 μm) after incubation with 0.2 mL of human serum spiked with 0.2 μg of Myo. There are many unknown peaks observed. Spectra were obtained through two days of independent experiments. Ab, antibody; HSA, human serum albumin.

When we compared the relative amount of Myo enriched from the serum samples, the MGMs exhibit the highest peak intensity of Myo compared with the other commercial beads (**Fig. 1-10**). The MGMs show about seven-fold higher peak intensities than the 2 μm and 7.9 μm beads (~12400 beads) do despite the amount of loaded antibodies is similar to each other (**Fig. 1-11**). Although the Dynabeads were able to hold more than twofold antibodies (~68 ng), the relative peak intensity of Myo was fourfold lower than the one from the MGMs. When we adjusted the surface area by increasing the number of beads up to ~44600, the 7.9 μm beads could carry threefold antibodies (~95 ng), while showing about a half of the MGMs peak intensity. Therefore, we confirmed that the MGMs exceptionally enriched the target antigen in serum samples even with the least amount of antibodies among the beads tested. This may be attributed to the effective isolation of the polymer core from the bulk serum proteins using SAM-Au layer; the van der Waals interaction of the aliphatic carbon chains induces a dense packing of the SAM molecules [43] and thereby provide high-density PEG groups sufficient for the suppression of nonspecific binding of serum proteins. [44]

Indeed, the density of the carboxyl groups of the PEG-alkanethiolates on MGMs was determined to be 9.2×10^{14} molecules cm^{-2} by colorimetric method (**Fig. 1-17**), [45] about two-fold higher than the density of typical alkanethiolate SAMs on flat Au surface [46,47] and PEG-alkanethiolate SAMs on Au nanoparticles. [48] This extraordinary density of PEG molecules can be ascribed to the uneven nanoparticular surface structure of the MGMs that extends accessible surface area (**Fig. 1-18**). In comparison, the density of carboxyl groups of the 7.9 μm magnetic polymer beads was four-fold higher than the one of the MGMs, which is roughly in agreement with the ratio of the amount of the immobilized antibody (**Fig. 1-11**). The 15 μm beads have two-fold lower carboxyl contents than the MGMs, comparable to the normal carboxyl alkanethiol SAM on flat Au surface.

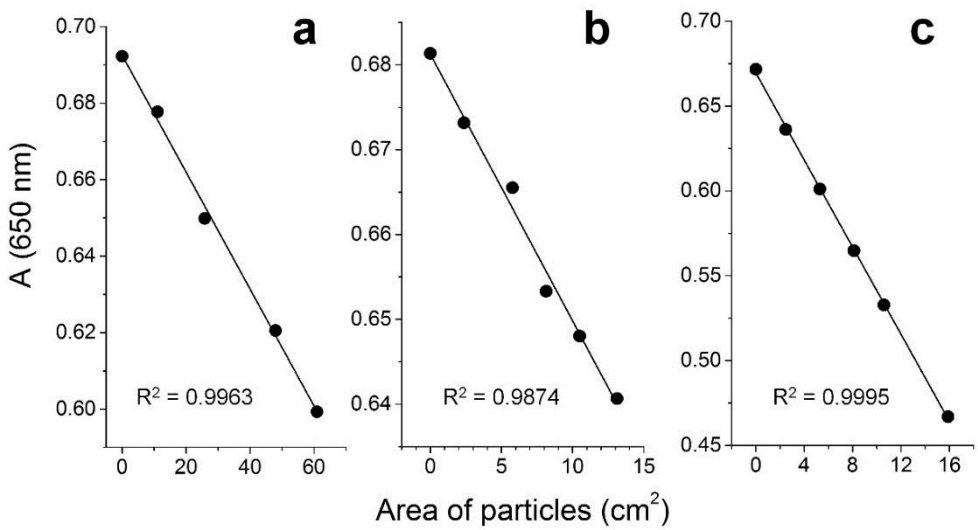

d

Bead type	Carboxyl group (molecules/cm^2)
15 μm polymer beads	4.3×10^{14} (5.1×10^{15} in the certificate of analysis)
15 μm MGMs	9.2×10^{14}
7.9 μm magnetic beads	3.8×10^{15}

Fig. 1-17. Determination of the amounts of surface carboxyl group. Plot of the absorbance at 650 nm versus the area of 15 μm polymer beads (a), 15 μm MGMs (b), and 7.9 μm magnetic beads (c). d) The density of surface carboxyl groups of each microbeads is tabulated.

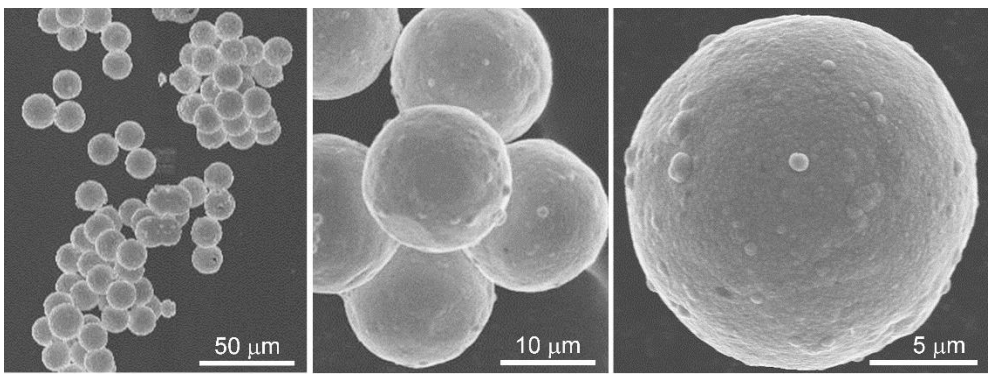

Fig. 1-18. FE-SEM images of MGMs 15 μm in diameter.

The formation of PEG-alkanethiolate SAM on the MGMs was further analysed by X-ray photoelectron spectroscopy (XPS) (**Fig. 1-19**) and attenuated total reflectance-Fourier transform infrared (ATR-FTIR) spectra (**Fig. 1-20**). The C1s XPS spectrum of the bare MGMs exhibits three species of C–C, C–O, and C=O, originating from the chemical ingredients used for the synthesis of MGMs, at 284.5, 285.8, and 288.4 eV, respectively (**Fig. 1-19a**). [49] After treating the MGMs with carboxyl-terminated PEG-alkanethiolates, the peak for C–O at 284.5 eV increased and two distinct peaks for C–C=O and O–C=O appeared at 287.4 and 288.8 eV, respectively, indicating the formation of carboxyl PEG layer on the MGMs (**Fig. 1-19b**). ATR-FTIR spectra of the bare and SAM-protected MGMs also show very similar results to the XPS data; strong increases of the absorption bands near 1140 and 1720 cm^{-1}, representing the C–O stretching of the PEG groups and the C=O stretching of the carboxylic groups (**Fig. 1-20**).

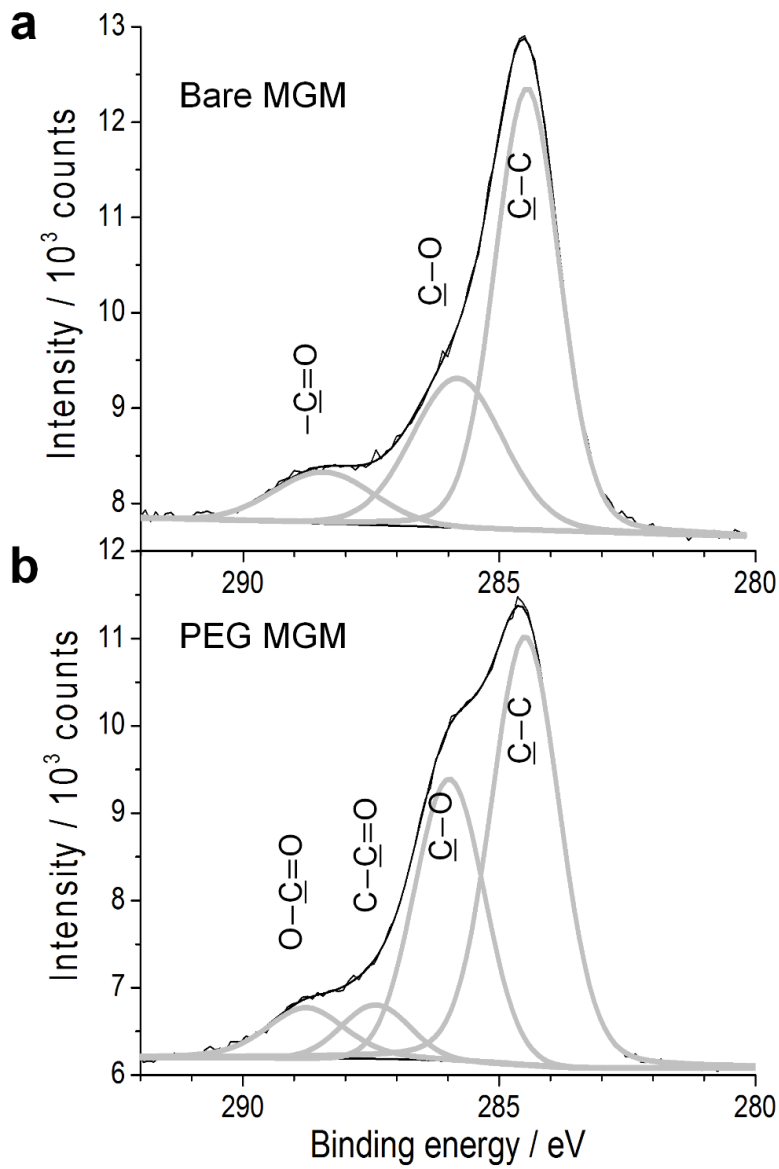

Fig. 1-19. C1s XPS spectra of a bare surface of MGMs (a) and the MGMs treated with carboxyl-terminated PEG-alkanethiolates (b).

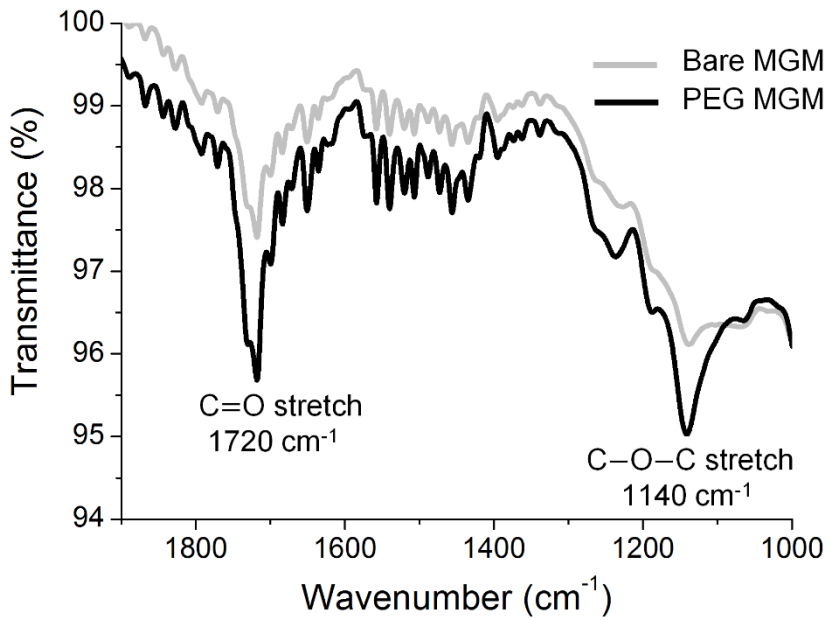

Fig. 1-20. Attenuated total reflectance-Fourier transform infrared (ATR-FTIR) spectra of bare MGMs (gray line) and the MGMs treated with carboxyl-terminated PEG-alkanethiolates (solid line).

We then conducted quantification of Myo in human sera using MGMs and MALDI-TOF MS to verify the potential use of the MGMs for clinical diagnosis. **Fig. 1-21a** shows representative MALDI mass spectra obtained from the MGMs incubated with serum samples spiked with Myo ranging 0.5-200 ng mL^{-1}. As shown in **Fig. 1-21b**, the standard curve obtained from three independent experiments shows a good linear relationship (R^2 = 0.9930). The empirical limit of detection (LOD) is 0.5 ng mL^{-1} (0.25 ng in 0.5 mL of serum sample) with 13.4 of signal-to-noise ratio. This subnanogram LOD of the MGMs using intact serum is quite promising in that the mass spectrometry-based immunoassays using magnetic nano- or microparticles require either PBS or diluted serum as incubation media while giving no better than 1-5 ng of detection limits. [11-13,16]

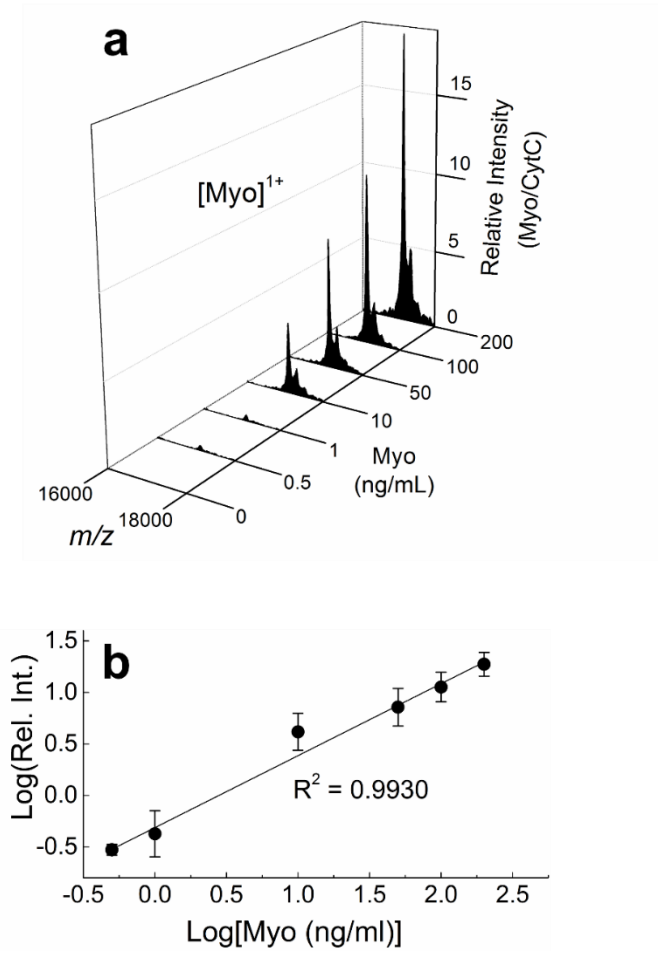

Fig. 1-21. Quantitative analysis of biomarkers in intact serum. Representative MALDI-TOF mass spectra with a serial dilution of Myo (a) in human serum. The standard calibration curve of Myo is shown in (b). Throughout the experiments, CytC was used as an internal standard. The error bars represent the standard deviations of three independent measurements.

We additionally quantified other serum biomarkers such as PSA and CK-MB to broaden the feasibility of the MGMs in protein enrichment. Unlike the Myo antibody, the antibodies for PSA and CK-MB, when immobilized onto protein G, failed to enrich the antigens probably because of less strong binding of mouse IgG1 isotype to protein G (**Fig. 1-22**). Only when we directly conjugate the antibodies with the SAM molecules on MGMs using EDC/NHS chemistry do we observe CK-MB and PSA in human sera with 10 and 25 ng mL^{-1} of detection limit, respectively (**Fig. 1-23 and 1-24 and Table 1**). In contrast, without protein G mediator, we failed to enrich any of the antigens using 7.9 and 15 μm microspheres (data not shown). That the MGMs can forgo the protein G mediation itself augurs well for their approach to physiological fluid in which plenty of human serum antibodies possibly replace the protein G-bound input antibodies.

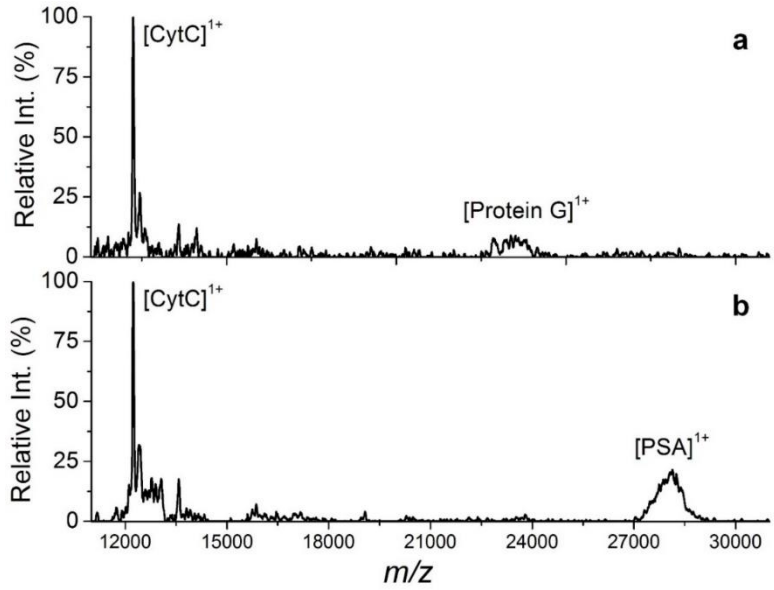

Fig. 1-22. Representative baseline-corrected MALDI-TOF mass spectra of antibody-modified MGMs after immunoreactions with 0.5 mL human serum spiked with 50 ng PSA. a) The IgG proteins were immobilized onto MGMs in an orientation-controlled manner via protein G affinity. b) The IgG proteins were conjugated to the SAMs on MGMs in a random orientation manner via covalent bond.

Unlike rabbit IgG that has strong binding to protein G, the IgG1 isotype of mouse anti-PSA antibody has moderate affinity to protein G.

(http://www.millipore.com/techpublications/tech2/binding_properties, accessed Feb. 2014)

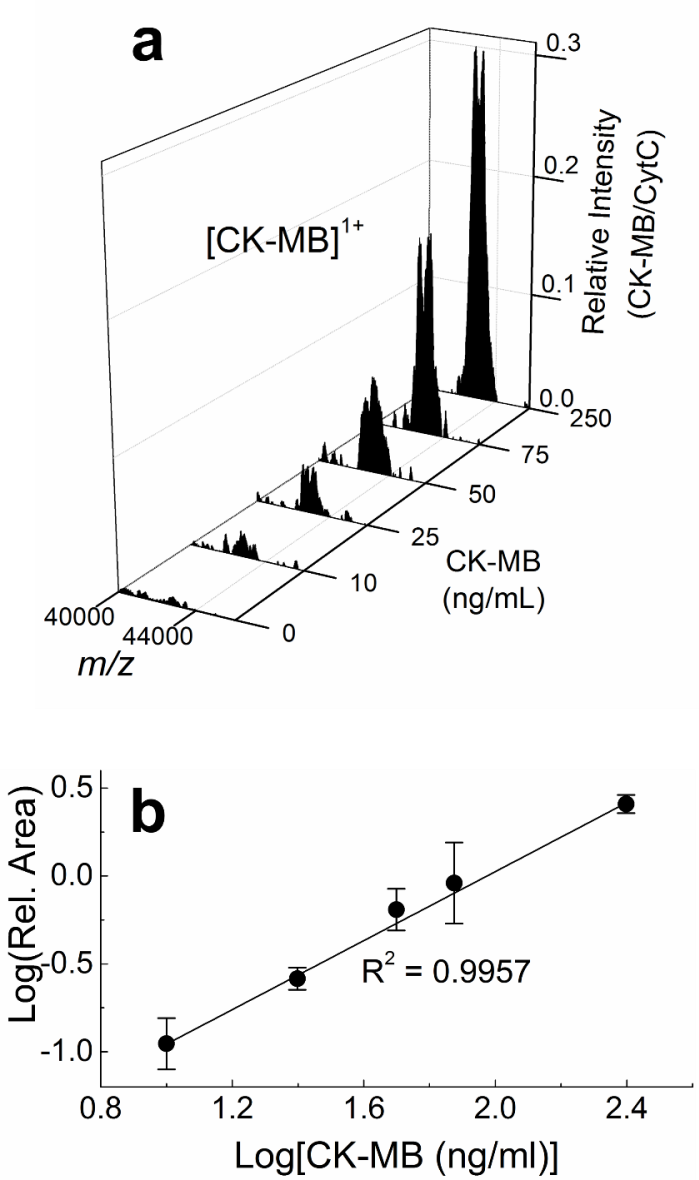

Fig. 1-23. Representative MALDI-TOF mass spectra with a serial cocentration of CK-MB in human serum (a). The standard calibration curve of CK-MB (b) is shown below.

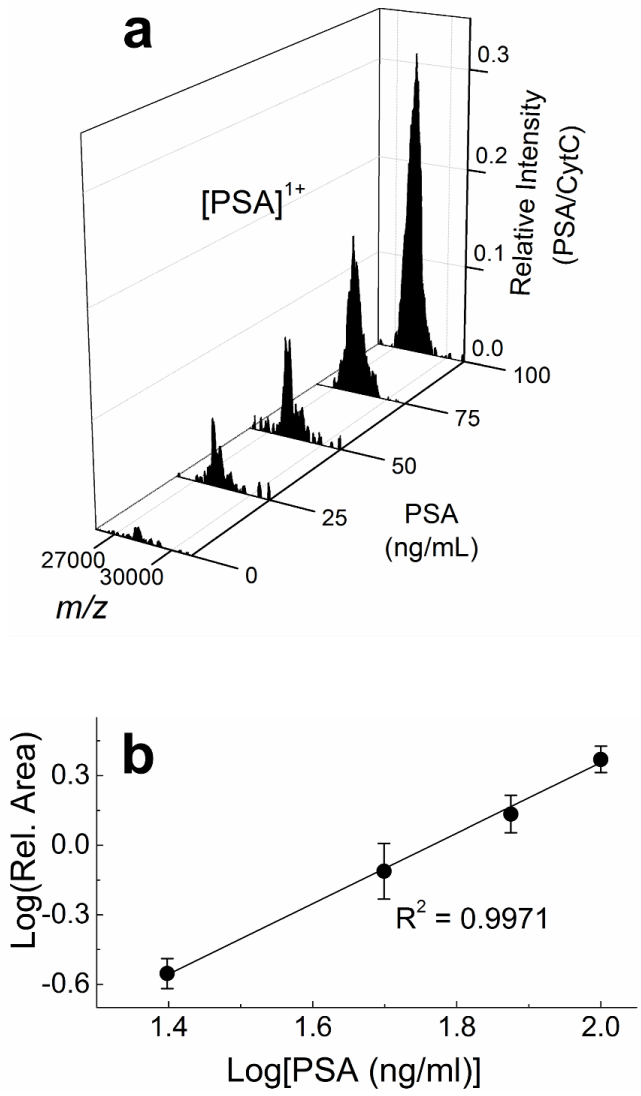

Fig. 1-24. Representative MALDI-TOF mass spectra of PSA with a serial dilution in human serum (a). The standard calibration curve of PSA is shown in (b).

Table 1. Detection limits and signal to noise ratios of the three biomarkers quantified using the MGMs and MALDI-TOF MS.

	Biomarkers (ng/mL)		
	Myo	CK-MB	PSA
Upper limit of quantification	200	250	100
Limit of detection†	0.5	10	25
Signal to noise‡	13	8.2	19

†Empirical values well above the blank signal + 3SD (standard deviation)

‡Based on root-mean-square (RMS)

By taking advantage of innate ability of MALDI MS in simultaneous identification of multiple macromolecules, we performed multiplex detection of all three biomarkers spiked in human serum. For this experiment, we modified the MGMs with antibodies for Myo, PSA, and CK-MB without protein G. As expected, all three antigens dominantly appeared in the mass spectra without any accompanying serum proteins, consolidating the anti-fouling ability of the MGMs (Fig. 1-25 and 1-26).

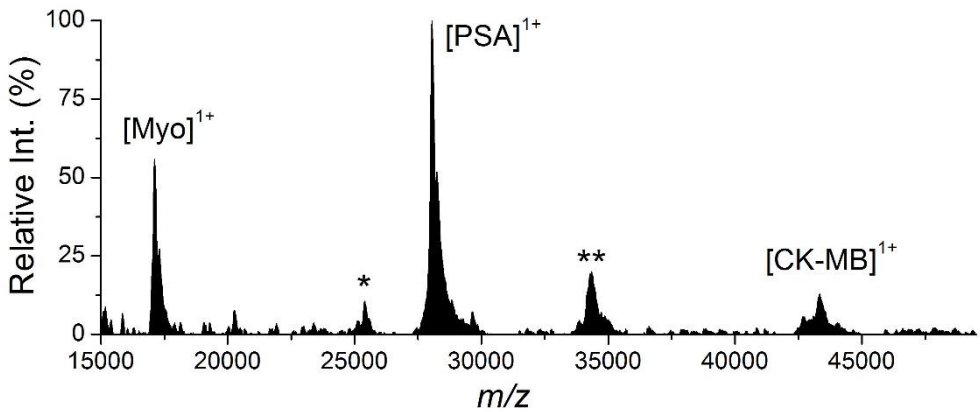

Fig. 1-25. MALDI-TOF mass spectrum for multiplex analysis obtained from 0.5 mL human serum spiked with 25 ng Myo, 50 ng PSA, and 50 ng CK-MB. The peaks at 26 (*) and 34 kDa (**) originate from antibodies.

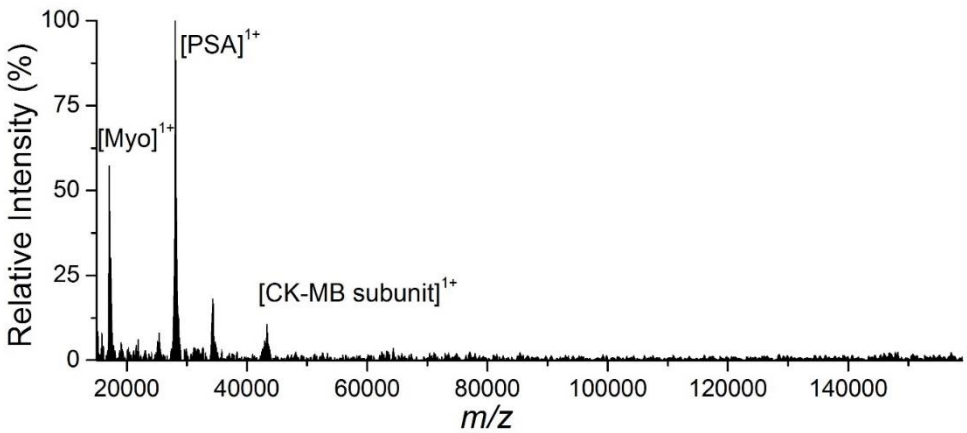

Fig. 1-26. Baseline-corrected whole-range MALDI-TOF mass spectra for multiplexed detection of Myo, CK-MB, and PSA.

1.4. Conclusions

The successful integration of suspension arrays with label-free detection methods will undoubtedly ensure a forefront technology for multiplex assays. However, only a highly effective prevention of nonspecific binding would realise clinical approach of such label-free assays. The Au surface layer of the MGMs enables facile formation of PEG-SAM molecules, efficiently preventing nonspecific adsorptions owing to the dense packing of SAM molecules and thus make erroneous serum dilution obsolete (**Fig. 1-27**). Thus, the Au-coated microspheres render label-free detection of multiple biomarkers by merging the benefits of MALDI MS and functional SAM-Au layers, paving the fundamental path for the rapid multiplexed immunoassays.

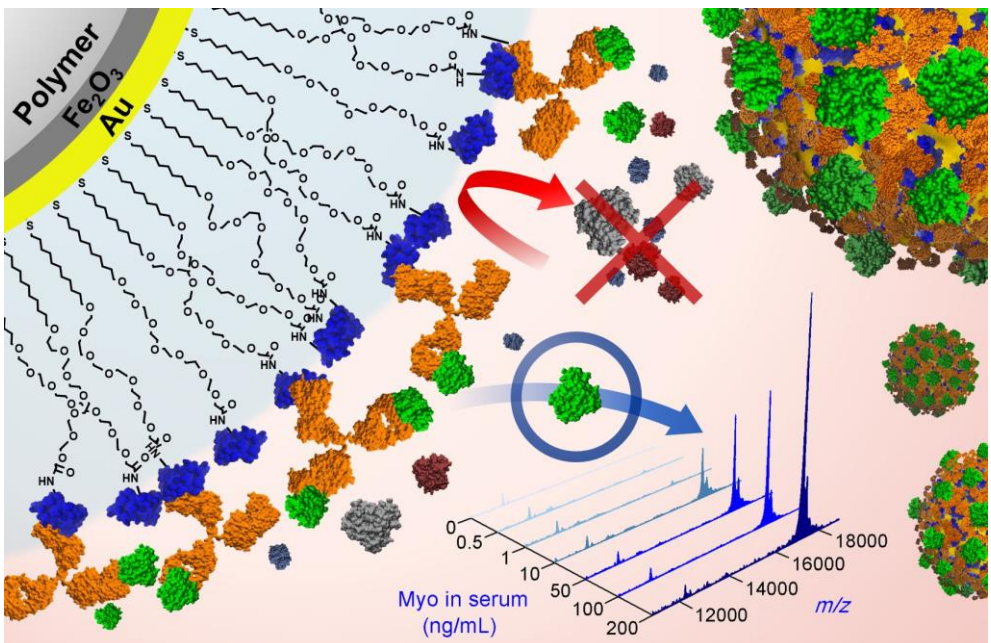

Fig. 1-27. A mass-based label-free detection of blood biomarkers under physiological conditions is realised using gold-plated magnetic polymer microspheres covered with self-assembled monolayers of polyethylene glycol alkanethiolates that effectively prevent heavy nonspecific binding of serum proteins.

2.5. References

[1] L. Hartwell, D. Mankoff, A. Paulovich, S. Ramsey and E. Swisher, *Nat. Biotechnol.*, 2006, **24**, 905–908.

[2] A. Csordas, A. E. Gerdon, J. D. Adams, J. R. Qian, S. S. Oh, Y. Xiao and H. T. Soh, *Angew. Chem., Int. Edit.*, 2010, **49**, 355–358.

[3] J. F. Rusling, *Anal. Chem.*, 2013, **85**, 5304–5310.

[4] N. L. Anderson and N. G. Anderson, *Mol. Cell. Proteomics*, 2002, **1**, 845–867.

[5] R. Etzioni, N. Urban, S. Ramsey, M. McIntosh, S. Schwartz, B. Reid, J. Radich, G. Anderson and L. Hartwell, *Nat. Rev. Cancer*, 2003, **3**, 243–252

[6] L. Thadikkaran, M. A. Siegenthaler, D. Crettaz, P. A. Queloz, P. Schneider and J. D. Tissot, *Proteomics*, 2005, **5**, 3019–3034

[7] B. Pesch, T. Bruning, G. Johnen, S. Casjens, N. Bonberg, D. Taeger, A. Muller, D. G. Weber and T. Behrens, *Biochim. Biophys. Acta*, 2014, **1844**, 874–883.

[8] Y. J. Zhao, X. W. Zhao, J. Hu, M. Xu, W. J. Zhao, L. G. Sun, C. Zhu, H. Xu and Z. Z. Gu, *Adv. Mater.*, 2009, **21**, 569–572.

[9] Y. J. Zhao, X. W. Zhao, J. Hu, J. Li, W. Y. Xu and Z. Z. Gu, *Angew.*

Chem., Int. Edit., 2009, **48**, 7350-7352

[10] G. Z. Deng, K. Xu, Y. Sun, Y. Chen, T. S. Zheng and J. L. Li, *Anal. Chem.*, 2013, **85**, 2833-2840.

[11] P. C. Lin, P. H. Chou, S. H. Chen, H. K. Liao, K. Y. Wang, Y. J. Chen and C. C. Lin, *Small*, 2006, **2**, 485-489.

[12] K. Y. Wang, S. A. Chuang, P. C. Lin, L. S. Huang, S. H. Chen, S. Ouarda, W. H. Pan, P. Y. Lee, C. C. Lin and Y. J. Chen, *Anal. Chem.*, 2008, **80**, 6159-6167.

[13] P. C. Lin, S. H. Chen, K. Y. Wang, M. L. Chen, A. K. Adak, J. R. R. Hwu, Y. J. Chen and C. C. Lin, *Anal. Chem.*, 2009, **81**, 8774-8782

[14] E. Stern, A. Vacic, N. K. Rajan, J. M. Criscione, J. Park, B. R. Ilic, D. J. Mooney, M. A. Reed and T. M. Fahmy, *Nat. Nanotechnol.*, 2010, **5**, 138-142.

[15] Y. S. Lin, P. J. Tsai, M. F. Weng and Y. C. Chen, *Anal. Chem.*, 2005, **77**, 1753-1760.

[16] Chou, S. H. Chen, H. K. Liao, P. C. Lin, G. R. Her, A. C. Y. Lai, J. H. Chen, C. C. Lin and Y. J. Chen, *Anal. Chem.*, 2005, **77**, 5990-5997.

[17] L. Zhao, H. Q. Qin, Z. Y. Hu, Y. Zhang, R. A. Wu and H. F. Zou, *Chem. Sci.*, 2012, **3**, 2828-2838.

[18] Y. R. Ma, X. L. Zhang, T. Zeng, D. Cao, Z. Zhou, W. H. Li, H. Y. Niu and Y. Q. Cai, *ACS Appl. Mater. Inter.*, 2013, **5**, 1024–1030.

[19] C. S. Raska, C. E. Parker, S. W. Sunnarborg, R. M. Pope, D. C. Lee, G. L. Glish and C. H. Borchers, *J. Am. Soc. Mass Spectr.*, 2003, **14**, 1076–1085.

[20] E. N. Warren, P. J. Elms, C. E. Parker and C. H. Borchers, *Anal. Chem.*, 2004, **76**, 4082–4092.

[21] J. Jiang, C. E. Parker, J. R. Fuller, T. H. Kawula and C. H. Borchers, *Anal. Chim. Acta*, 2007, **605**, 70–79.

[22] Y. Li, J. S. Wu, D. W. Qi, X. Q. Xu, C. H. Deng, P. Y. Yang and X. M. Zhang, *Chem. Commun.*, 2008, DOI: Doi 10.1039/B716055k, 564–566.

[23] Y. Liu, Y. Li, J. Y. Liu, C. H. Deng and X. M. Zhang, *J. Am. Soc. Mass Spectr.*, 2011, **22**, 2188–2198.

[24] J. P. Nolan and L. A. Sklar, *Trends Biotechnol.*, 2002, **20**, 9–12.

[25] H. Y. Hsu, T. O. Joos and H. Koga, *Electrophoresis*, 2009, **30**, 4008–4019.

[26] Y. Rosenberg–Hasson, L. Hansmann, M. Liedtke, I. Herschmann and H. T. Maecker, *Immunol. Res.*, 2014, **58**, 224–233.

[27] C. D. Walkey, J. B. Olsen, H. B. Guo, A. Emili and W. C. W. Chan, *J. Am. Chem. Soc.*, 2012, **134**, 2139-2147.

[28] N. Tang, P. Tornatore and S. R. Weinberger, *Mass. Spectrom. Rev.*, 2004, **23**, 34-44.

[29] T. B. Martins, B. M. Pasi, C. M. Litwin and H. R. Hill, *Clin. Diagn. Lab. Immun.*, 2004, **11**, 325-329.

[30] S. Pang, J. Smith, D. Onley, J. Reeve, M. Walker and C. Foy, *J. Immunol. Methods*, 2005, **302**, 1-12.

[31] T. Waterboer, P. Sehr and M. Pawlita, *J. Immunol. Methods*, 2006, **309**, 200-204.

[32] T. Bryan, X. L. Luo, L. Forsgren, L. A. Morozova-Roche and J. J. Davis, *Chem. Sci.*, 2012, **3**, 3468-3473.

[33] T. Bryan, X. L. Luo, P. R. Bueno and J. J. Davis, *Biosens. Bioelectron.*, 2013, **39**, 94-98.

[34] X. L. Luo, M. Y. Xu, C. Freeman, T. James and J. J. Davis, *Anal. Chem.*, 2013, **85**, 4129-4134.

[35] C. S. Jeon, I. Hwang and T. D. Chung, *Adv. Funct. Mater.*, 2013, **23**, 1484-1489.

[36] A. Chiu, W. K. Chan, S. H. Cheng, C. K. Leung and C. H. Choi,

Qjm-Mon. J. Assoc. Phys., 1999, **92**, 711-718.

[37] M. I. Mohammed and M. P. Y. Desmulliez, *Lab. Chip*, 2011, **11**, 569-595.

[38] J. V. Staros, R. W. Wright and D. M. Swingle, *Anal. Biochem.*, 1986, **156**, 220-222.

[39] H. Neubert, E. S. Jacoby, S. S. Bansal, R. K. Iles, D. A. Cowan and A. T. Kicman, *Anal. Chem.*, 2002, **74**, 3677-3683.

[40] P. Peluso, D. S. Wilson, D. Do, H. Tran, M. Venkatasubbaiah, D. Quincy, B. Heidecker, K. Poindexter, N. Tolani, M. Phelan, K. Witte, L. S. Jung, P. Wagner and S. Nock, *Anal. Biochem.*, 2003, **312**, 113-124.

[41] A. Kausaite-Minkstimiene, A. Ramanaviciene, J. Kirlyte and A. Ramanavicius, *Anal. Chem.*, 2010, **82**, 6401-6408.

[42] J. Su and M. Mrksich, *Angew. Chem., Int. Edit.*, 2002, **41**, 4715-4718.

[43] J. C. Love, L. A. Estroff, J. K. Kriebel, R. G. Nuzzo and G. M. Whitesides, *Chem. Rev.*, 2005, **105**, 1103-1169.

[44] S. R. Sheth and D. Leckband, *Proc. Natl. Acad. Sci. U.S.A.*, 1997, **94**, 8399-8404.

[45] A. Hennig, A. Hoffmann, H. Borcherding, T. Thiele, U. Schedler and U. Resch-Genger, *Anal. Chem.*, 2011, **83**, 4970-4974.

[46] L. H. Dubois and R. G. Nuzzo, *Annu. Rev. Phys. Chem.*, 1992, **43**, 437-463.

[47] P. Li, J. J. Xu, Q. Wang and C. Wu, *Langmuir*, 2000, **16**, 4141-4147.

[48] H. Hinterwirth, S. Kappel, T. Waitz, T. Prohaska, W. Lindner and M. Lammerhofer, *ACS Nano*, 2013, **7**, 1129-1136.

[49] R. E. Ducker, S. Janusz, S. Q. Sun and G. J. Leggett, *J. Am. Chem. Soc.*, 2007, **129**, 14842-14843.

2. A New Transdermal Drug Delivery System Using a Disposable Reverse Electrodialysis Patch as Electrical Power Source

2.1 Introduction

Transdermal drug delivery is an attractive alternative to oral route and parenteral injections. [1−3] In contrast to traditional routes such as oral delivery, transdermal delivery bypasses the hepatic first−pass elimination and chemical degradations in the gastrointestinal tract. When compared with hypodermic injections which generate dangerous medical waste, transdermal delivery can afford self−administration and longtime release of drugs while relieving pain during administration of therapeutic agents due to the non−invasive nature. However, despite of many advantages, low permeability of human skin limits choice of drugs applicable for the transdermal route. It is well known that the stratum corneum (SC), the outermost layer of the skin possessing multilamellar lipid bilayers that fill the interspaces between corneocytes, functions as a strong protective

layer in order to maintain homeostasis. Therefore, most of drugs capable of penetrating the SC are small molecules (a few Daltons) and only active at a very low concentration in blood such as a few ng/mL or less. [1-5]

Reverse electrodialysis (RED) is a promising technology generating eco-friendly electrical power from renewable resources. About 80 mV can be obtained from mixing entropy based on the assumption of 100% permselectivity when an ion-exchange membrane (IEM) is in between river water (e.g. 0.017 M NaCl) and sea water (e.g. 0.50 M NaCl) which are inexhaustible supplies in estuaries. Unlike solar generation governed by weather conditions, the RED system is able to produce relatively stable electrical power. However, power production from RED is still insufficient to replace part of current electrical power, e.g. fossil fuel- and nuclear-based power generation, because of low power density [6-8] although there have been keen efforts to date since the first report in the early 1950s. [9] On the other hand, eco-friendly RED system holds a great potential in application for where only low electrical power requires such as bio/chemical sensors and potable medical devices.

Manufacturing a miniaturized RED requires a very simple process, piling up cation- and anion-exchange membranes alternatively. Additionally, an initial voltage of RED desired can be readily generated by adjusting the salinity ratio of the feed solutions and the number of IEMs in the system. In this regard, we supposed that a miniaturized RED as electrical power source would be applicable for transdermal drug delivery system.

The unique way of the power generation process also allows RED system suitable for transdermal drug delivery. In general, the RED power production in a large scale, there should be electrodes at the ends of the cell to convert the ionic current to the electrical current for an external use. However, in case of RED for the transdermal drug delivery, the current conversion process is unnecessary because both of RED and biological system comprise only ionic current in principle. Thus, the metal electrodes that cause side effects on the skin would be unnecessary in combination of RED system with transdermal drug delivery. Here, we demonstrate a new concept of transdermal drug delivery system based on RED as electrical power source (**Fig. 2-1**).

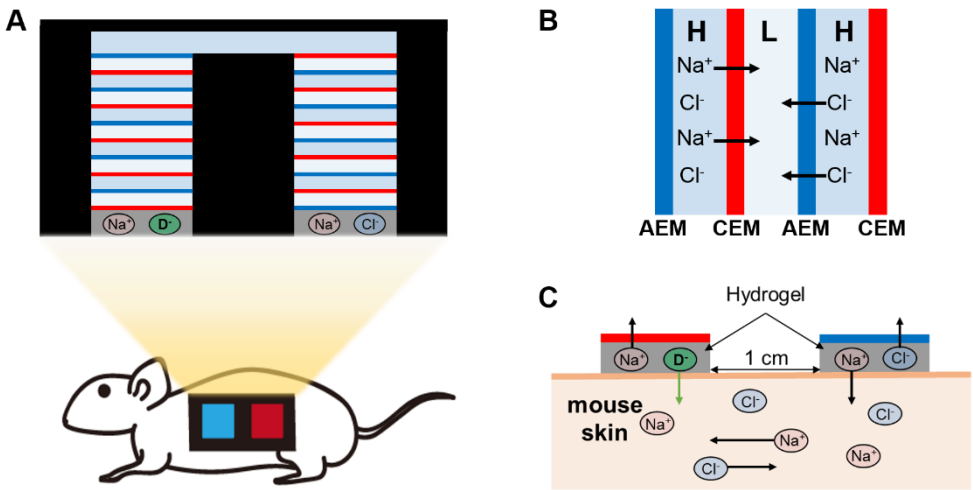

Fig. 2-1. A new transdermal drug delivery system based on RED. (A) Schematic representation of the RED patch attached on mouse skin. (B) Selective ion flows from a high-concentrate (H) NaCl solution to a low-concentrate (L) one through anion-exchange membranes (AEMs) and cation-exchange membranes (CEMs). (C) The negatively charged drug (D^-) penetrates the mouse skin while the sodium ion moves towards the L solution through the CEM to maintain electrical neutrality in the hydrogel matrix.

2.2. Experimental Section

2.2.1. Materials

Ketorolac tromethamine (KT), lidocaine hydrochloride (LID), risedronate monosodium (RIS), sodium chloride, acrylamide, *N,N'* −methylenebisacrylamide, and 2,2′ −azobis(2−methylpropionamidine) dihydrochloride were purchased from Sigma−Aldrich (St. Louis, MO, USA). Selemion CMV and AMV were purchased from Asashi Glass Co., Ltd. Double−sided waterproofing tape was from ACE cross SBX, Japan. The 22 G sterile hypodermic needle were bought from Kovax−Syringe; Korea vaccine co., Ltd., Korea. High performance liquid chromatography (HPLC)−grade solvents were obtained from J.T. Baker (Mallinckrodt Baker, Inc., Phillipsburg, NJ). Deionized water (Barnstead Nano−pure Diamond, 18.2 MΩ/cm of resistance) was used in all experiments.

2.2.2. Fabrication of reverse electrodialysis (RED) patch

Schematic illustration of the RED patch with 10 cell pairs was shown in Fig. 2−7. A cell pair, the repeating unit in RED patch, is composed of two layers of the double−sided waterproofing tape, one

cation exchange membrane (CEM), one anion exchange membrane (AEM), and spacers. Double-sided waterproofing tape (thickness: 250 μm/a layer, length: 2.0 cm, width: 4.0 cm) has two square holes (1.0 × 1.0 cm^2) inside separated from each other by a distance of 1 cm. An AEM and a CEM were cut in squares (1.5 × 1.5 cm^2) and attached on each square hole of the tape. Every square hole in the double-sided waterproofing tape were filled with two nonconductive fabric spacers (1.0 × 1.0 cm^2) between the membranes. The 22 G sterile hypodermic needles were put into the every hole between the IEMs for the injection of NaCl solution. After 10 cell pairs were piled in an alternating pattern, 3-layered double-sided waterproofing tape with a rectangular hole inside (3.0 × 1.0 cm^2) and 3-layered long spacer (3.0 × 1.0 cm^2) were attached onto the uppermost floor. Finally, the top of the RED stack is covered with OHP film (4.0 × 2.0 cm^2). In the lowest floor, two layers of the double-sided waterproofing tape was added for hydrogel gel loading afterward. The 4.4 M and 0.011 M NaCl solutions were injected into the every hole space via the needles alternatively. The uppermost space was filled with 4.4 M NaCl solution for high ionic conductivity.

2.2.3. Energy recovery

$$\Delta G_{mix} = (\Delta G_c + \Delta G_d - \Delta G_b)$$

$$\Delta G_{mix} = \sum [c_{i,c} V_c RTln(a_{i,c})] + [c_{i,d} V_d RTln(a_{i,d})] - [c_{i,b} V_b RTln(a_{i,b})]$$

$a_{i,x}$ = Activity of NaCl solutions,

V_c = 0.05 (1 × 1 × 0.05 cm^3) × 4 = 0.2 cm^3, V_d = 0.05 × 3 = 0.15 cm^3,

V_b = 0.05 × 7 = 0.35 cm^3, R = 8.314 $\frac{j}{mol \cdot k}$, T = 298.15 [k]

$$\Delta G_c = 2\left\{0.51\frac{mol}{L} \cdot 0.2 \times 10^{-3} L \cdot 8.314\frac{J}{mol \cdot k} \cdot 298.15 kln 0.51 \times 0.683\right\} = -0.532923\, J$$

$$\Delta G_d = 2\left\{0.017\frac{mol}{L} \cdot 0.15 \times 10^{-3} L \cdot 8.314\frac{J}{mol \cdot k} \cdot 298.15 kln 0.017 \times 0.878\right\} = -0.0531552\, J$$

$$\Delta G_b = 2\left\{0.2987\frac{mol}{L} \cdot 0.35 \times 10^{-3} L \cdot 8.314\frac{J}{mol \cdot k} \cdot 298.15 kln 0.2987 \times 0.709\right\} = -0.804507\, J$$

$$\Delta G_{mix} = (\Delta G_c + \Delta G_d - \Delta G_b) = 0.218423\, J$$

22.4% energy recovery obtained by calculating the ratio of power produced over the measured time (5.56 h in this study) to the amount of theoretical free energy (0.218 J) at initial conditions.

2.2.4. Preparation of hydrogels

Hydrogels as drug reservoirs were prepared for the attachment onto the skin. The 30% (w/v) polyacrylamide is synthesized using acrylamide (monomer), *N,N'*−methylenebisacrylamide (cross linker), and 2,2′ −azobis(2−methylpropionamidine) dihydrochloride

(initiator). Drug compounds and NaCl were added into the monomer solutions for drug loading part and for the counterpart, respectively. The 150 μL monomer solutions were placed on the glass molds to provide square-shaped gels (1.0 × 1.0 cm^2) and baked on a hot plate at 100 ℃. The polyacrylamide hydrogels as made with moderate moisture were cooled and then put on the lowest IEMs. Positively charged drug-containing hydrogels were placed on the CEM side, otherwise negatively charged drug-containing hydrogels were on the AEM side.

2.2.5. HPLC analysis

Ketorolac, risedronate, and lidocaine were analyzed using the HPLC (1200, Agilent, USA). [18-20] The HPLC system was composed of a binary pump with a detector set to 262 nm for risedronate, 314 nm for ketorolac and 230 nm for lidocaine, respectively. All chromatographic separation was achieved with Agilent symmetry C18, 150 mm × 4.6 mm, 5 μm column. Flow rate was 1 mL/min and injection volume was 25 μL. All samples were analyzed for 30 min. Risedronate was quantified with the mobile

phase containing a mixture of 5 mM sodium pyrophosphate and 5 mM tetra-*n*-butyl ammonium hydrogen bromide at pH 7.0 and acetonitrile with the ratio of 93:7. Ketorolac was analyzed in the conditions with the mobile phase containing a mixture of 0.1M ammonium acetate buffer (pH4.0) and acetonitrile with the ratio of 75:25. LID was analyzed with the mobile phase containing a mixture of aqueous 0.1 M sodium dihydrogen phosphate and 5 mM tetra-*n*-butyl ammonium hydroxide and methanol with the ratio of 60:40.

2.2.6. *In vitro* skin permeation test

Eight week old C57BL/6 mice were purchased from Orient Bio, Inc. (Seoungnam, Gyeonggi, Korea). Just before the experiment, the mice were sacrificed and full-thickness skins were obtained. Then, the subcutaneous fat and subdermal tissues were removed carefully. The inside of the skin was washed with phosphate buffered saline (PBS) solution slightly, then attached to square-type Franz diffusion cell with the area of 1.5 × 3.5 cm^2 and the volume of 7 mL. The square-type Franz diffusion cell was manufactured autonomously for the suitable combination with the RED patch. PBS (0.9% sodium

chloride) was used as a receptor medium. The RED patch and passive diffusion patch with the drug-containing hydrogels were attached to the mice skins. During the administration (15, 30, 45, 60, 90, and 120 min), 0.3 mL aliquots were collected from the receptor medium in the diffusion cell while replenishing the same amount of fresh PBS solution. The receptor medium was stirred with a magnetic bar at 200 rpm and 37 ±1 ℃. For monitoring real time current, digital multimeter (DMM) connected to the RED patch was used. After the experiment, the RED patches were detached from the skin and the remaining voltage of the RED was measured. The remaining amount of drugs in the skin was extracted using 0.1 M HCl in PBS solution for 48 h. The animal care committee of Seoul National University approved *in vivo* animal study and all samples were analyzed by using HPLC.

2.2.7. *In vivo* animal test: Ovariectomized mouse model

Fourteen week old C57BL/6N mice were purchased from KOATECH (Gyeonggi-do, Korea). The experiments were carried out in accordance with the Institutional Animal Care and Use Committees of Kyungpook National University. Animals were

maintained on a 12-h light: 12-h darkness cycle at 22-25°C in specific pathogen-free (SPF) conditions and fed with standard rodent chow and water. We performed ovariectomy (OVX) and sham-OVX (SHAM) surgery to induce osteoporosis. [13] The OVX group was divided into OVX (OVX), 0.02% RIS delivery based on passive diffusion (0.02% DF), 0.02% RIS delivery based on the RED patch (0.02% RED), 0.002% RIS delivery based on passive diffusion (0.002% DF), and 0.002% RIS delivery based on the RED patch (0.002% RED). Seven to eight numbers of mice were used for every group. Before applying the patch with the drugs, the hair on the flank side (2.5 X 4.5 cm^2) of the mouse was shaved carefully with an electric shaver 4 days after surgery. Only RIS-loaded hydrogel patches or the RED patches with RIS-loaded hydrogel were attached to the shaved region on each mouse retained under anesthetization for 1 h. The total dose of RIS in the hydrogel was 30 μg for 0.02% and 3 μg for 0.002%. The RIS administration was conducted every 10 days, 3 times totally. The SHAM group was treated with the drug-free hydrogels. After 10 days from the last administration of RIS, all mice were sacrificed and then the lumbar vertebras and femora were

extracted for bone analysis.

2.2.8. Micro-computed tomography (Micro-CT) analysis

To determine 3-dimensional bone structure, the fourth lumbar vertebrae and femur were scanned with Quantum FX micro CT (PerkinElmer, Waltham, MA) using the following settings: isotropic voxel size, 10 μm; tube voltage, 90 kVp; tube current, 160 mA; field of view, 5mm; scan time, 3 min. All morphometric parameters were calculated using Analyze 12.0 software. All nomenclature followed the guidelines of the American Society for Bone and Mineral Research.

2.2.9. Statistical analysis

We performed all the quantitative experiments at least in triplicate. The data were presented as mean values with standard errors. We assessed the statistical significance of the results by the two-tailed Student's *t* test for *in vitro* penetration test. Statistical significance of *in vivo* results was determined by one-way analysis of variance (ANOVA) with Bonferroni's test using GraphPad Prism 5.0 software.

$P \leq 0.05$ was considered to indicate significant differences.

2.3. Results and Discussion

To test feasibility of patch-type RED as electrical power source for the application of transdermal drug delivery, we manufactured a miniaturized RED patch (2×2×~0.35 cm^3) configured with 3 pairs of IEMs and 2 Ag/AgCl plate electrodes at the end of the stack (**Fig. 2-2**). Right after injection of NaCl solutions with the salinity ratio of 30 (0.017 and 0.51 M), the RED cell generated a reproducible initial voltage, 0.478 ±0.017 V, ~ 99.6% of theoretical voltage (0.48 V) on the assumption of 100% permselectivity of the IEMs(**Fig. 2-3**). The potential response of the RED in connection with 9.79 kΩ external resistor representing a skin resistance was monitored for 5.56 h. The RED patches as-made exhibited reproducible responses during the measurement time (**Fig. 2-4**). The potential variations mainly originated from the different amount of injected NaCl solutions, the source of the electrical energy. Produced electrical energy from the REDs was 0.0489 ±0.0062 J which was 22.4% energy recovery defined as the ratio of power produced over the measured time (5.56 h in this study) to the amount of theoretical free Gibbs energy (0.218 J) at initial conditions. The energy recovery value would vary with

the elapsed time and magnitude of external resistance connected to the RED system. An initial voltage of RED was directly proportional to the number of the IEMs used, showing very good linearity (R^2 = 1) (**Fig. 2-5**).

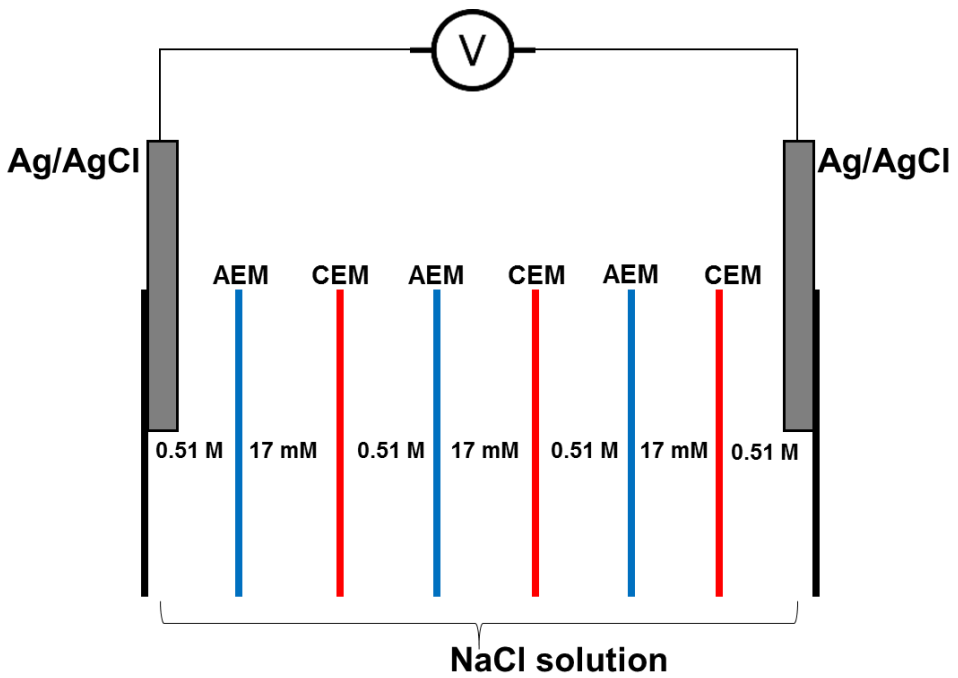

Fig. 2-2. The structure of the miniaturized RED patch consisting of 3 pairs of IEMs and Ag/AgCl electrodes at the ends of the cell for voltage response measurement.

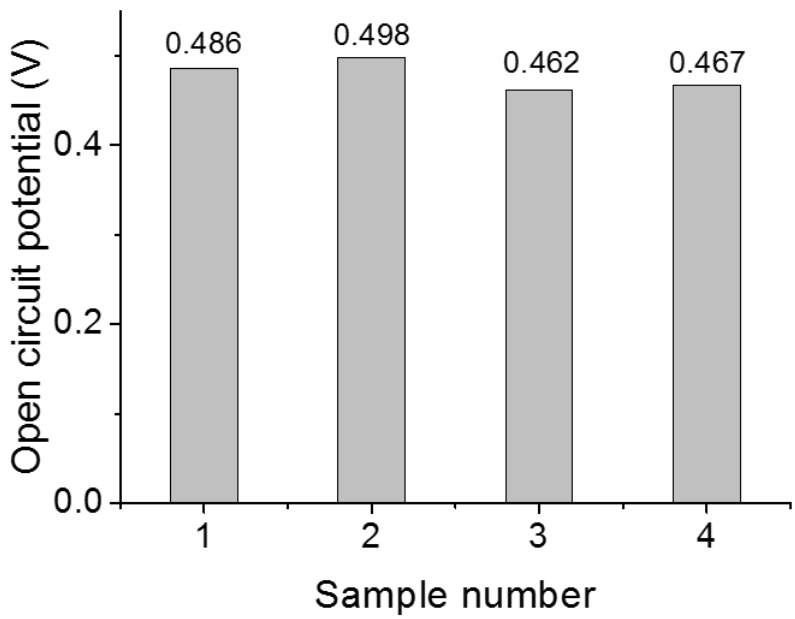

Fig. 2-3. Initial voltages of the REDs right after injection of NaCl solutions to the cell.

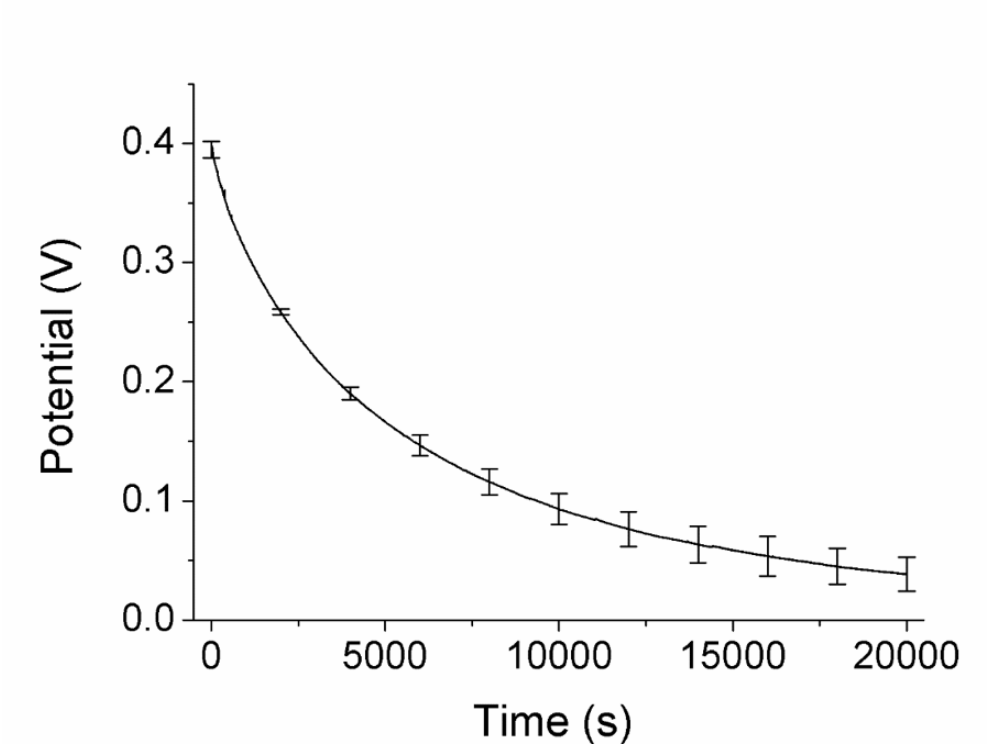

Fig. 2-4. Electrical characteristics of the miniaturized RED patches. Potential response of the RED patches with 9.79 kΩ external resistor. The error bars represent the standard deviations of three independent measurements.

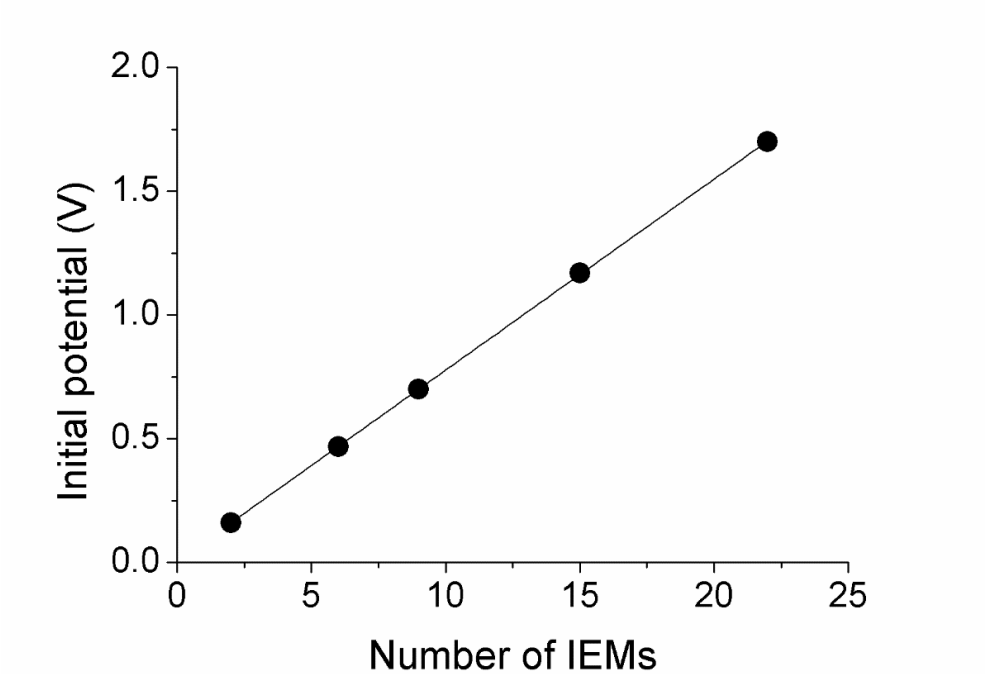

Fig. 2-5. Electrical characteristics of the miniaturized RED patches. Initial potential of the RED right after injection of NaCl solutions (0.017 and 0.51 M) with respect to the number of IEMs used in the cell.

We next modified the structure of the RED patch appropriate for transdermal drug delivery to introduce the generated electrical power into a biological system. Two lateral ends of an RED patch possessing different potentials (one side would be positive or negative potential against the other) should face to the same side for skin attachment. To do so, we devised an RED patch consisting of two columns in parallel with an electrically conducting path containing the H NaCl solution and the two ends of the RED patch present on the same side (**Fig. 2-1A**). This RED configuration enabled itself thin and flexible with a wide range of initial voltage (up to ~5.5 V with six parallel columns and the salinity ratio of 400, i.e. 0.011 and 4.4 M NaCl) (**Fig. 2-6**).

Before applying the RED system to transdermal drug delivery, the RED patch was further optimized, consisting of 2 parallel columns, 10 pairs of IEMs, and the salinity ratio of 400 (0.011 and 4.4 M NaCl) to produce appropriate electrical current (**Fig. 2-7 and 2-8**). The RED patch generated a reliable voltage (2.21 ±0.12 V) right after injection of the NaCl solutions. In theory, any charged drugs will be delivered through the skin using the RED system although

penetration rate critically depends on physicochemical properties of drugs such as molecular weight, partitioning coefficient and ionization degree. [2] Ketorolac (KT) and risedronate (RIS), anionic drugs, and lidocaine (LID), a cationic drug, were chosen as model drugs. KT and LID are a potent nonsteroidal anti-inflammatory drug (NSAID) and a topical anesthetic, respectively. RIS is used for clinical treatment of various metabolic bone diseases (e.g. osteoporosis) as an inhibitor of osteoclastic activity. [10] These drugs have low permeability through the skin under passive diffusion conditions and various side effects when administered via other routes, for example, oral delivery and hypodermic injections. [11] In particular, RIS has bioavailability less than 0.5% in the oral route and causes some serious side effects (e.g. abdominal pain, arthralgia, and osteonecrosis of the jaw). [12] Therefore, we selected these drugs to investigate the capability of the RED patch as potable power source for the application of transdermal drug delivery.

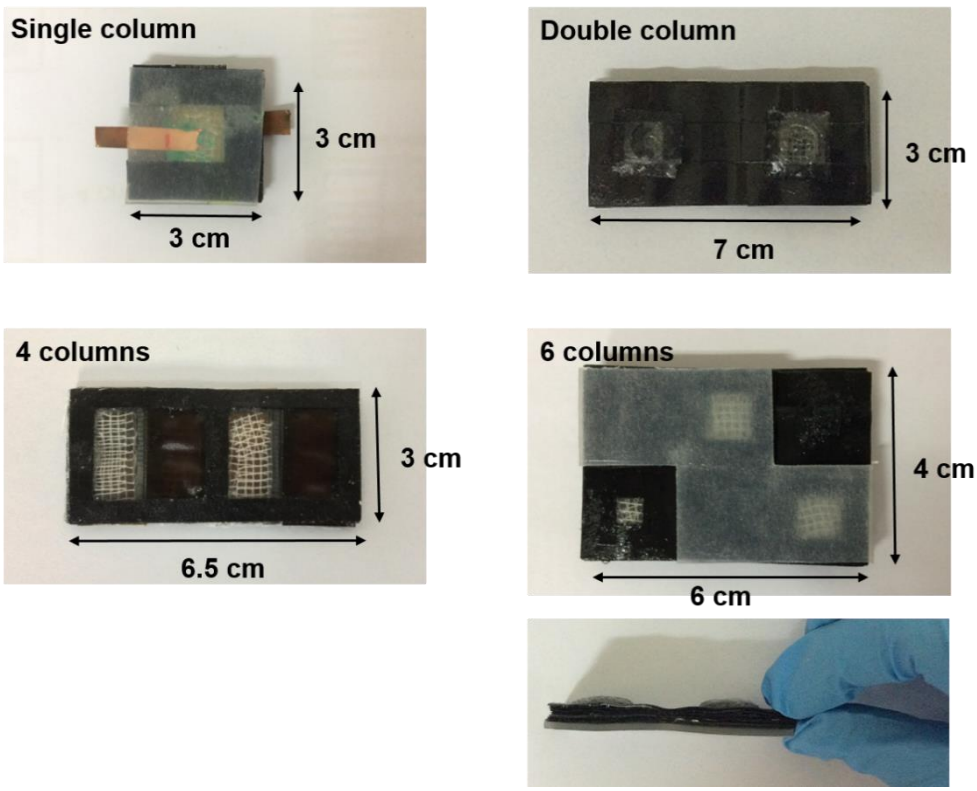

Fig. 2-6. Examples of RED patches with different configurations and sizes.

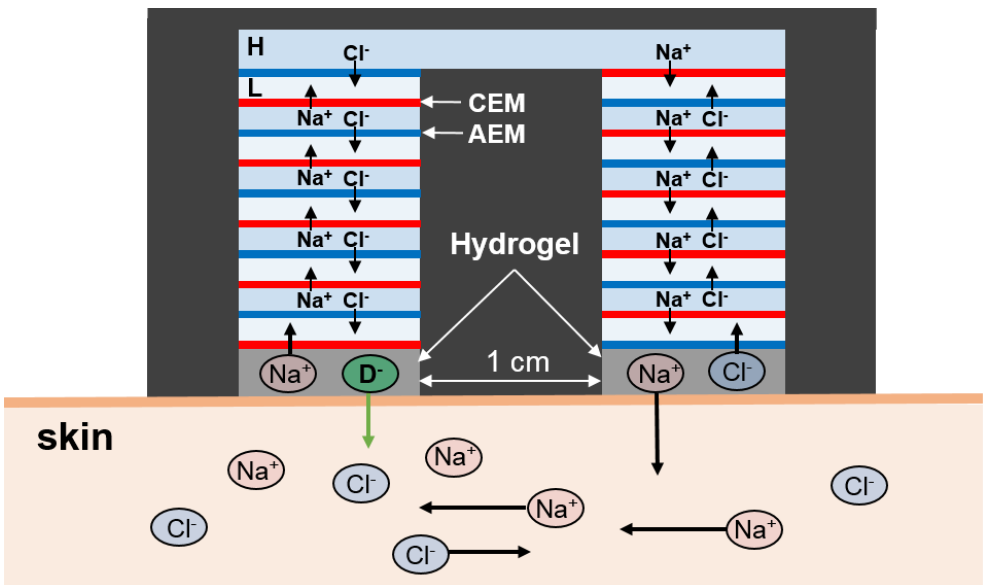

Fig. 2-7. Schematic representation of the patch type RED consisting of 10 pairs of ion-exchange membranes (IEMs). All solution layers between the IEMs is 500 μm thick except the uppermost layer (750 μm). The drug-loaded hydrogel (left side) possesses negative potential compared with 50 mM NaCl-containing hydrogel (right side). If the drug is positively charged, it should be in the right hydrogel and the other hydrogel contains only NaCl electrolyte.

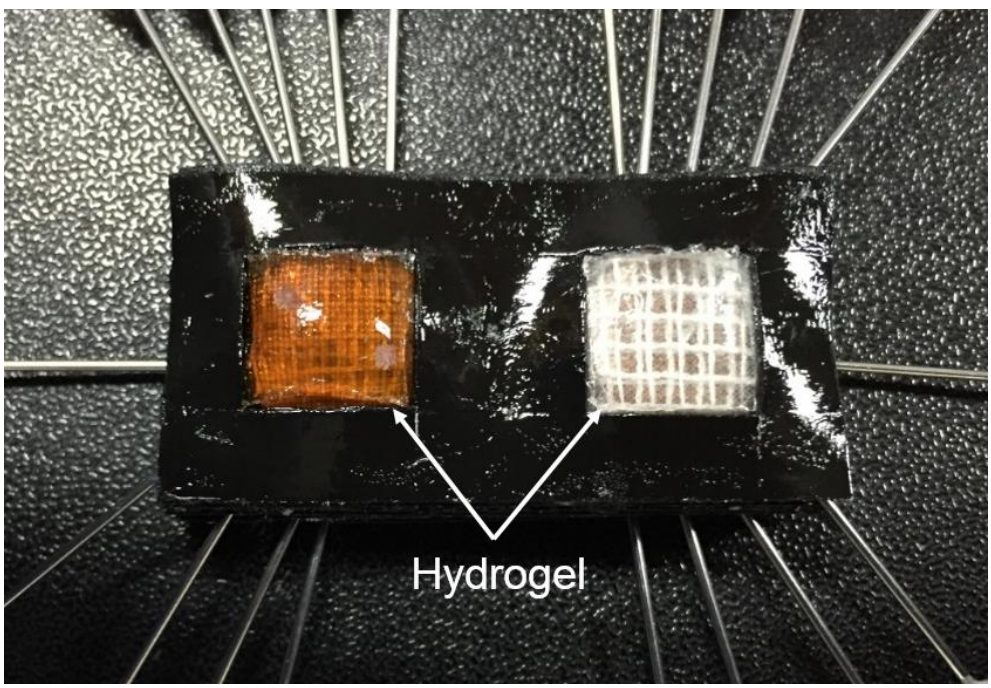

Fig. 2-8. An image of an RED patch as prepared.

The penetrated amount of KT from hydrogel matrix containing 2% (w/v) KT attached on mouse skin was 20.6 ±7.32 μg/cm^2 after 2 h diffusive (DF) administration while that with the RED patch was 408.3 ±75.07 μg/cm^2, ~20-fold higher than the DF delivery (**Fig. 2-9**). In case of residual KT in the skin, the RED group exhibited only ~2.4-fold higher amount than the DF administration (RED, 61.06 ± 7.28 μg/cm^2 and DF, 25.06 ± 1.50 μg/cm^2). Interestingly, the penetrated and residual amount of drugs were comparable in the DF condition, but much different in the condition of RED-based delivery.

Similar to the delivery results of KT, the penetrated amount from 2% (w/v) LID-containing hydrogel was ~9-fold greater in the RED group than in the DF delivery group (RED, 148.9 ± 28.68 μg/cm^2 and DF, 16.20 ± 7.69 μg/cm^2) while the residual amount in the skin was similar to each other (**Fig. 2-10**).

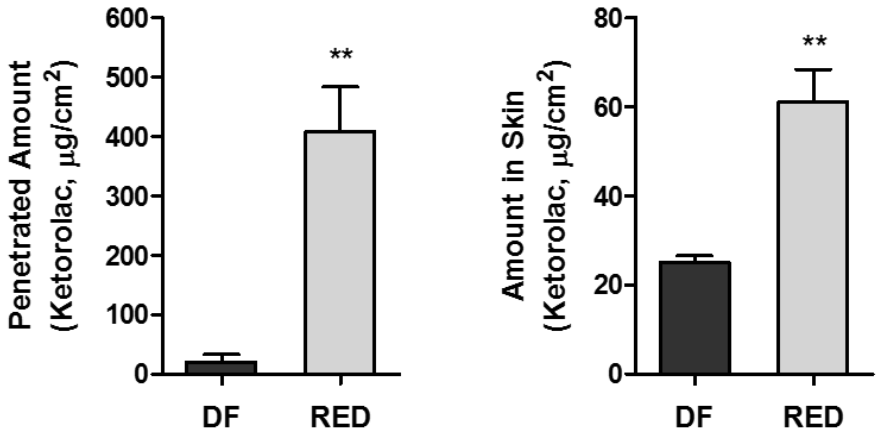

Fig. 2-9. *In vitro* penetration study of model drugs. Penetrated amounts of KT under condition of the DF delivery and active delivery with the RED system using freshly excised mouse skin (left). Comparison of remaining KT in the mouse skin after 2 h transdermal administration (right). The penetration tests were carried out using polyacrylamide hydrogel matrix containing 2% (w/v) drug. $^{**}P < 0.005$.

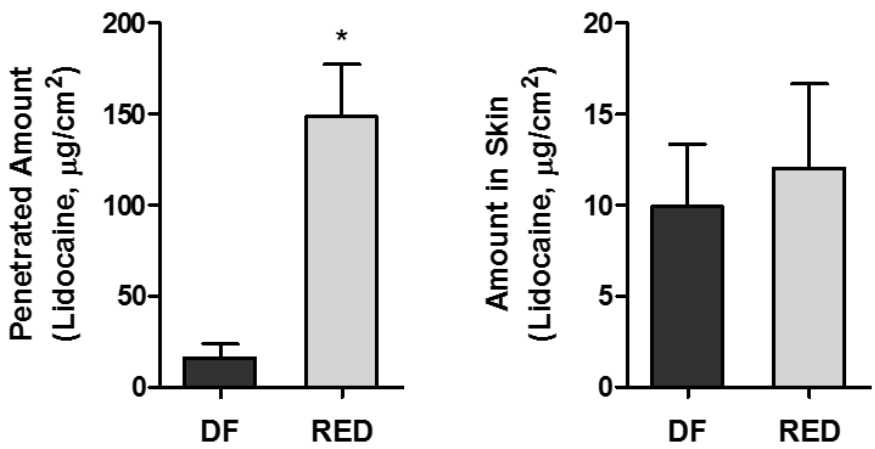

Fig. 2-10. *In vitro* penetration study of model drugs. Penetrated amounts of LID under condition of the DF delivery and active delivery with the RED system using freshly excised mouse skin (left). Comparison of remaining LID in the mouse skin after 2 h transdermal administration (right). The penetration tests were carried out using polyacrylamide hydrogel matrix containing 2% (w/v) drug. $*P < 0.05$.

We further conducted *in vitro* penetration test of RIS. Even though physicochemical properties of RIS, i.e. high hydrophilicity and iconicity in aqueous conditions, greatly hamper the skin penetration, remarkable increase was observed when administered by the means of the RED patches (**Fig. 2-11A**). The penetrated amount of RIS was ~36-fold higher with the RED patch than with the DF delivery (RED, 420.6 ± 98.00 μg/cm^2 and DF delivery, 11.67 ± 6.03 μg/cm^2). In the case of remaining RIS in the skin, the RED group showed only ~2-fold higher than the DF group (RED, 33.18 ± 7.15 μg/cm^2 and DF delivery, 14.78 ± 3.21 μg/cm^2) (**Fig. 2-11B**). The simultaneous response of current with time during the *in vitro* penetration experiment exhibited that the RED patch almost consumed its power within 1 h (**Fig. 2-11C and 2-12**). The accumulative amount of RIS penetrated agreed well with the current response, showing that ~85% of total amount was delivered within 1 h (358.2± 73.88 μg/cm^2). The *in vitro* penetration test using 0.2% (w/v) RIS-containing hydrogel was also conducted to monitor the concentration effect, resulting in ~15.3-fold higher in the RED group than in the DF group (2.37 ± 0.73 μg/cm^2 DF group and 36.3 ± 6.98 μg/cm^2 RED) (**Fig.**

2-13).

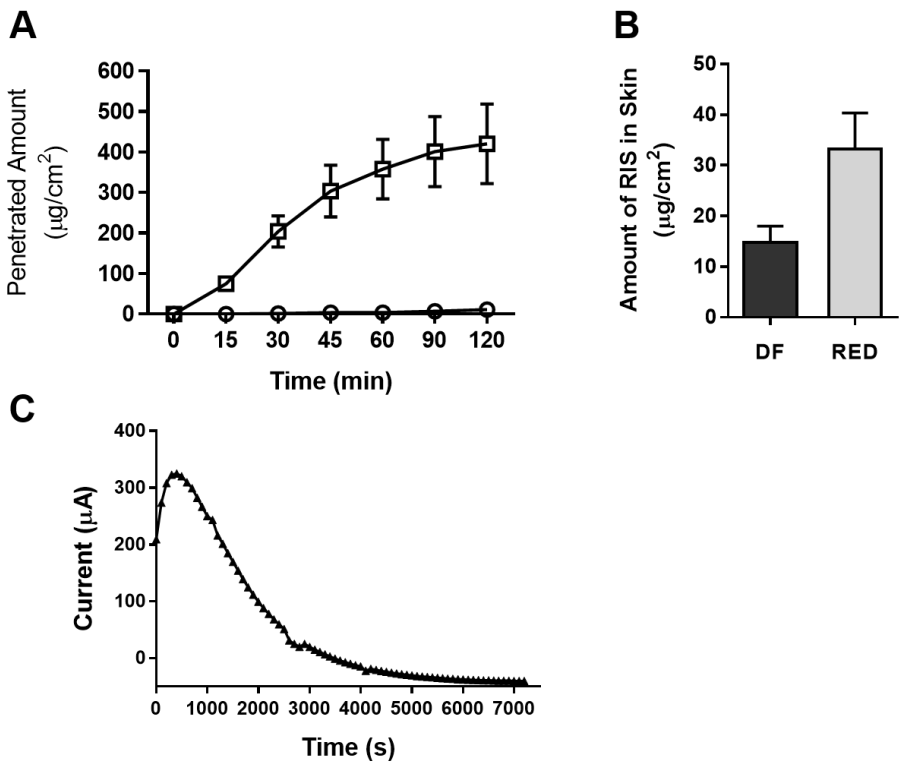

Fig. 2-11. *In vitro* penetration test of 2% (w/v) RIS under condition of passive diffusion (□) and active delivery with the RED patch (○). (A) Accumulative amount of RIS during 2 h administration. (B) Remaining amount of RIS in the skin after 2 h administration. (C) Current response of the RED patch during *in vitro* penetration test.

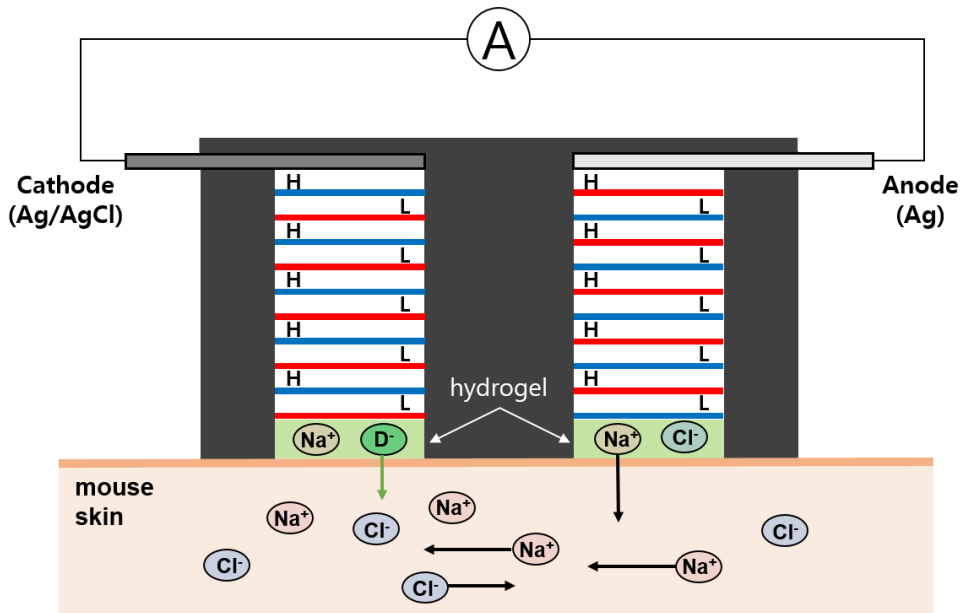

Fig. 2-12. The RED patch configured with the electrodes for the current measurement during drug administration.

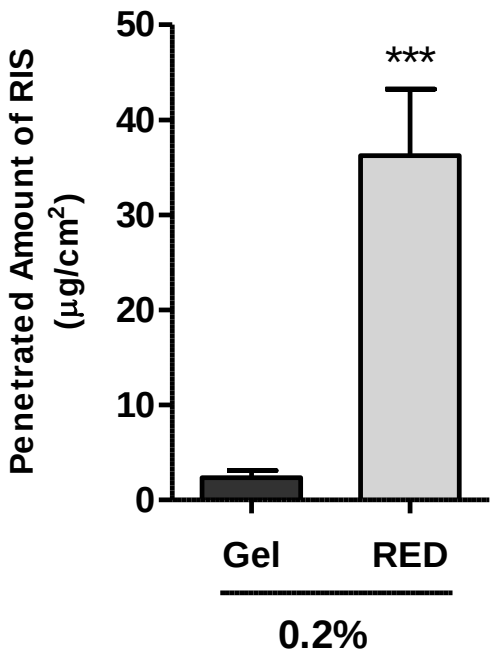

Fig. 2-13. *In vitro* penetration test of 0.2% (w/v) RIS. Graphs represent the total penetrated amount of RIS through the mouse skin for 2 h. ***$P < 0.0005$.

To study the effect of the electrodeless RED system on the penetration rate, an RED patch was fabricated with electrodes implanted into the both ends of the cell to relay the generated power externally and the other two electrodes connected to the RED were attached on the mouse skin with the RIS-loaded hydrogel matrix (**Fig. 2-14**). There was some difference observed in the penetrated amount from 2% RIS between the electrode-implanted RED (318.59 ± 59.86 μg/cm^2) and electrodeless RED (420.59 ± 98.00 μg/cm^2) (**Fig. 2-15**). In the case of 0.2% RIS delivery, the penetrated amount was ~3.4-fold higher in the electrodeless RED than in the electrode-implanted RED (electrodeless RED, 36.26 ±6.98 μg/cm^2 and RED with electrode, 10.57 ±4.34 μg/cm^2) (**Fig. 2-16**). The different efficiency in the drug delivery mainly stems from the results of faradaic reactions at the electrode producing competing ions (i.e. Cl^-) which has higher mobility than the drugs (i.e. RIS). Note that the difference in the penetrated amount between the RED systems was more distinct in 0.2% than in 2% RIS delivery because the generated competing ions (i.e. Cl^- in this study) more crucially affect the delivery efficacy due to higher concentration ratio of the competing

ions to the drugs in the hydrogel matrix. In addition, the competing charge effect will be greater with administration time.

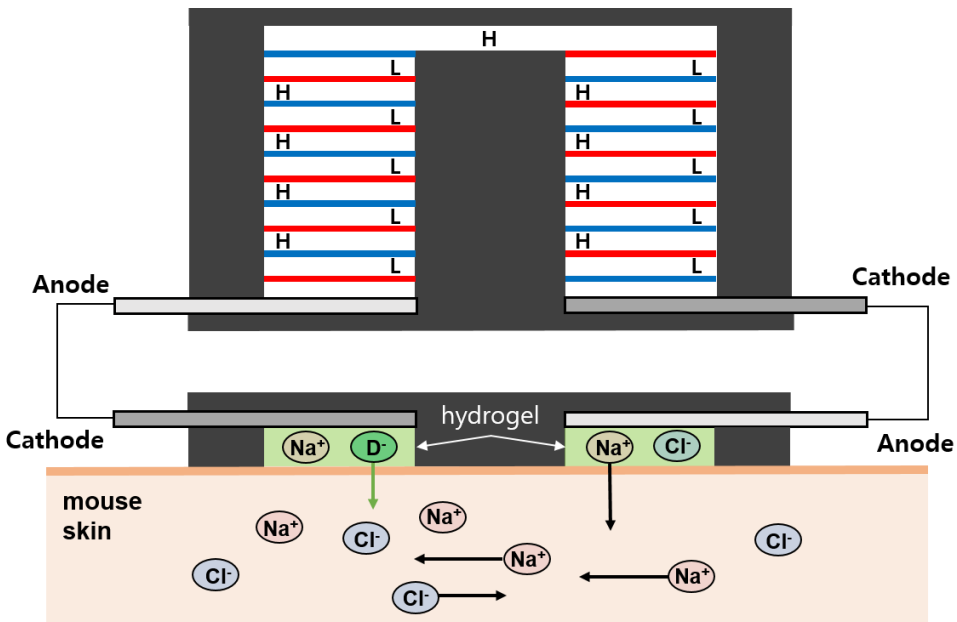

Fig. 2-14. Schematic illustration of the electrode-implanted RED patch representing a conventional battery.

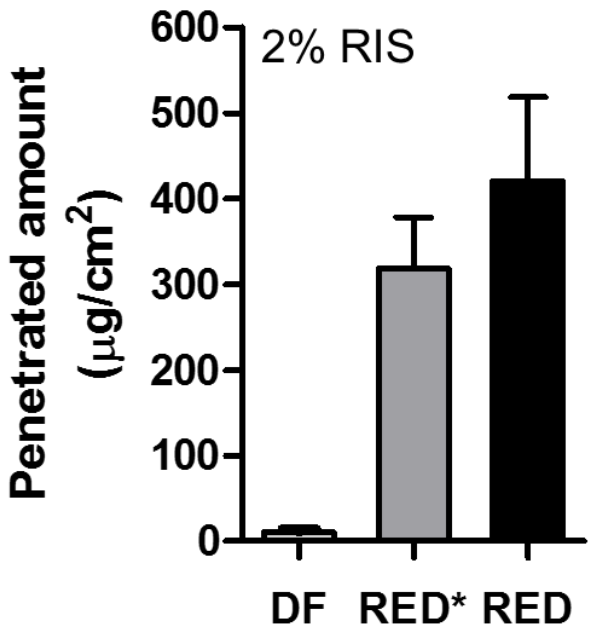

Fig. 2-15. The penetrated amounts from 2% RIS-containing hydrogel matrix after 2 h administration by using the DF delivery, electrode-implanted RED, and electrodeless RED.

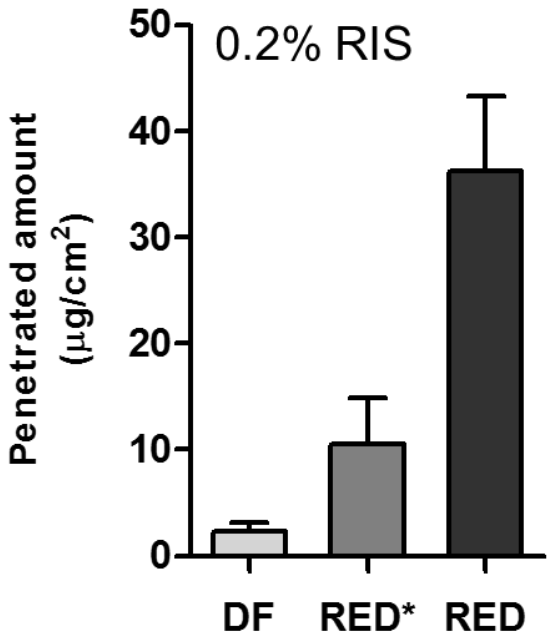

Fig. 2-16. The penetrated amounts from 0.2% RIS-containing hydrogel matrix after 2 h administration by using the DF delivery, electrode-implanted RED, and electrodeless RED.

To monitor *in vivo* therapeutic effect of topical application of RIS, we used estrogen-deficient osteoporosis mouse model. For comparison, 0.002 and 0.02% RIS was delivered by either passive diffusion or the RED patch (**Fig. 2-17**). The current response of the RED patch was monitored during the administration, showing very similar response to the *in vitro* measurement (**Fig. 2-18**). Among the representative images obtained by micro-computed tomography (Micro-CT) analysis, 0.02% RIS delivered by the RED patch presented greater bone formation of vertebrae than the ovariectomy (OVX) group and similar or even denser than the sham-OVX (SHAM) group (**Fig. 2-19**). Structural parameters of trabecular bone, i.e. bone volume per total volume (BV/TV), bone surface per bone volume (BS/BV), trabecular number (Tb.N), trabecular thickness (Tb.Th), and trabecular separation (Tb.Sp), was determined to quantify the therapeutic effects (**Fig. from 2-20 to 2-25**). Compared with the SHAM group, the OVX group exhibited significant changes in the bone parameters (16% decrease in BMD, 20% decrease in BV/TV, 20% increase in BS/BV, 11% decrease in Tb.Th , 8% increase in Tb.Sp, and 3% decrease in Tb.N), indicating that

successful induction of osteoporosis by OVX. In comparison with the OVX group, 0.02% RIS administration with the RED showed 37% increase in BMD, 48% increase in BV/TV, 18% decrease in BS/BV, 3% increase in Tb.Th , 23% decrease in Tb.sp, and 20% increase in Tb.N. All values appeared with the substantial differences except Tb.Th values. Similarly, 0.02% RED group also showed significant changes in all parameters compared with the DF delivery (e.g. 47% increase in BV/TV, 16 % decrease in BS/BV, 21% increase in Tb.N, and 24% decrease in Tb.Sp) that could not suppress the bone loss. Consequently, 0.02% RIS delivery by means of the RED afforded superior therapeutic effects on the osteoporosis-induced mouse.

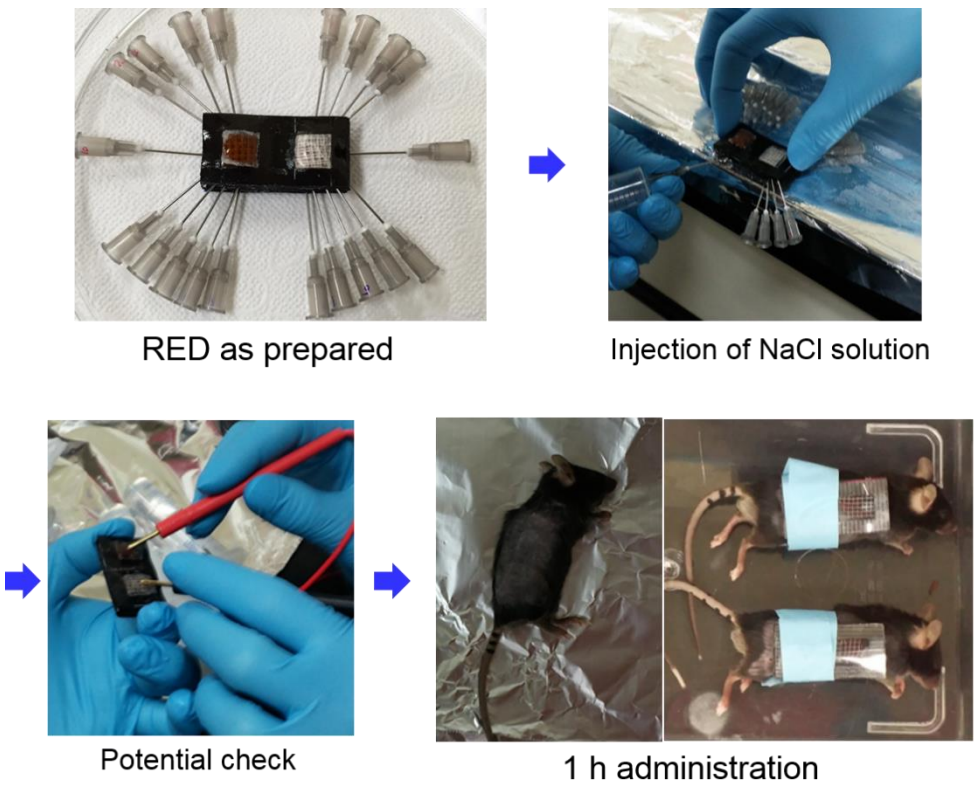

Fig. 2-17. The images showing the *in vivo* experimental process for administration of RIS.

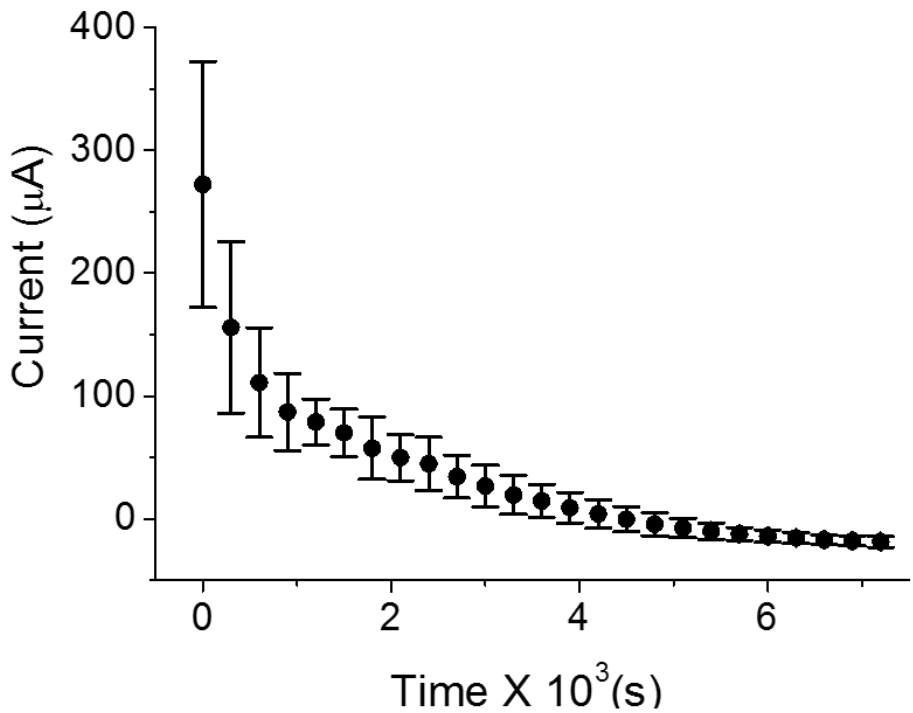

Fig. 2-18. The *in vivo* current response of RED patches during the administration of RIS.

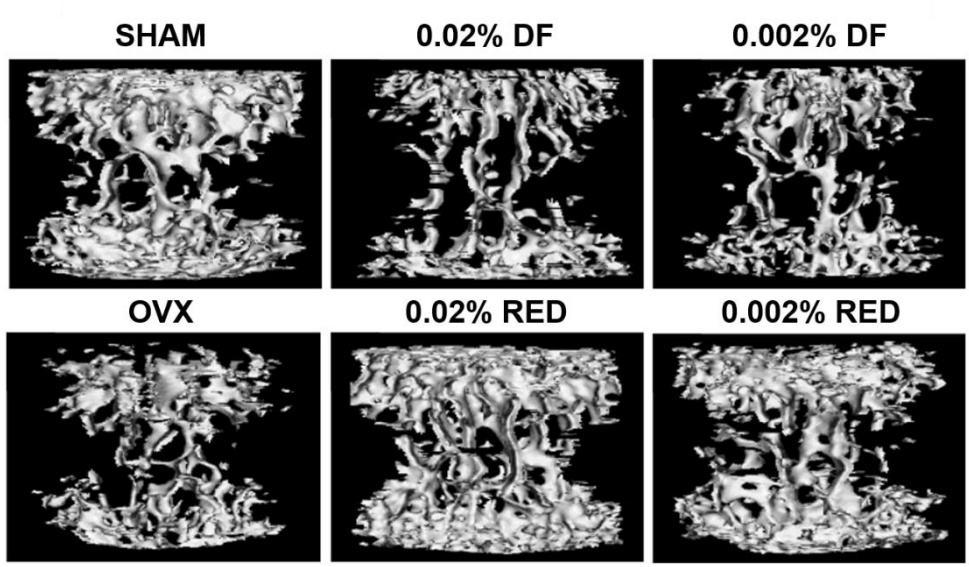

Fig. 2-19. Representative micro-CT images of vertebras showing the effect of RIS deliveries on ovariectomized mouse bones.

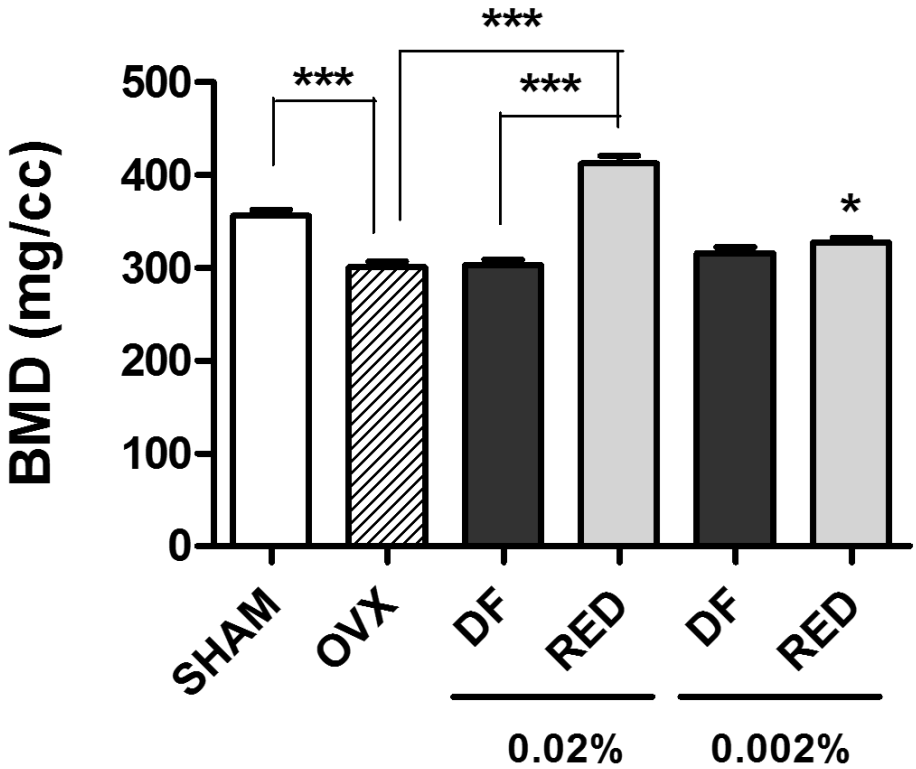

Fig. 2-20. Effect of RIS administration using the RED patch on ovariectomized mouse bone. Bone mineral density (BMD) in vertebras of the ovariectomized mice. $*P < 0.05$, $***P < 0.0005$.

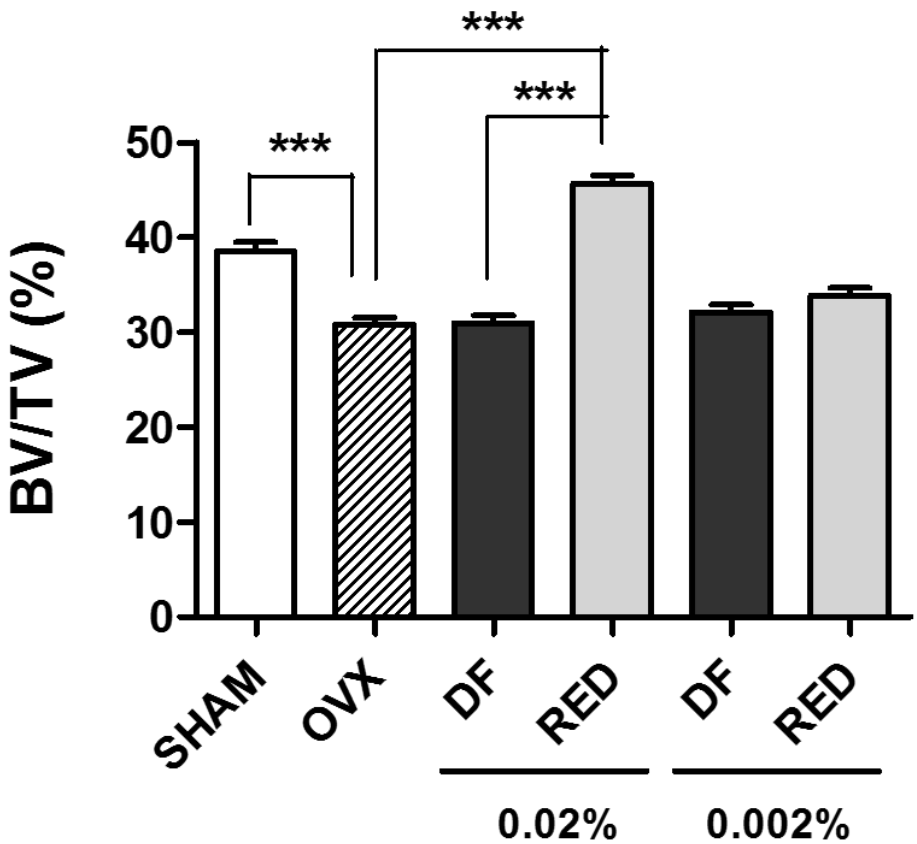

Fig. 2-21. Effect of RIS administration using the RED patch on ovariectomized mouse bone. Bone volume/total volume (BV/TV) in vertebras of the ovariectomized mice. ***$P < 0.0005$.

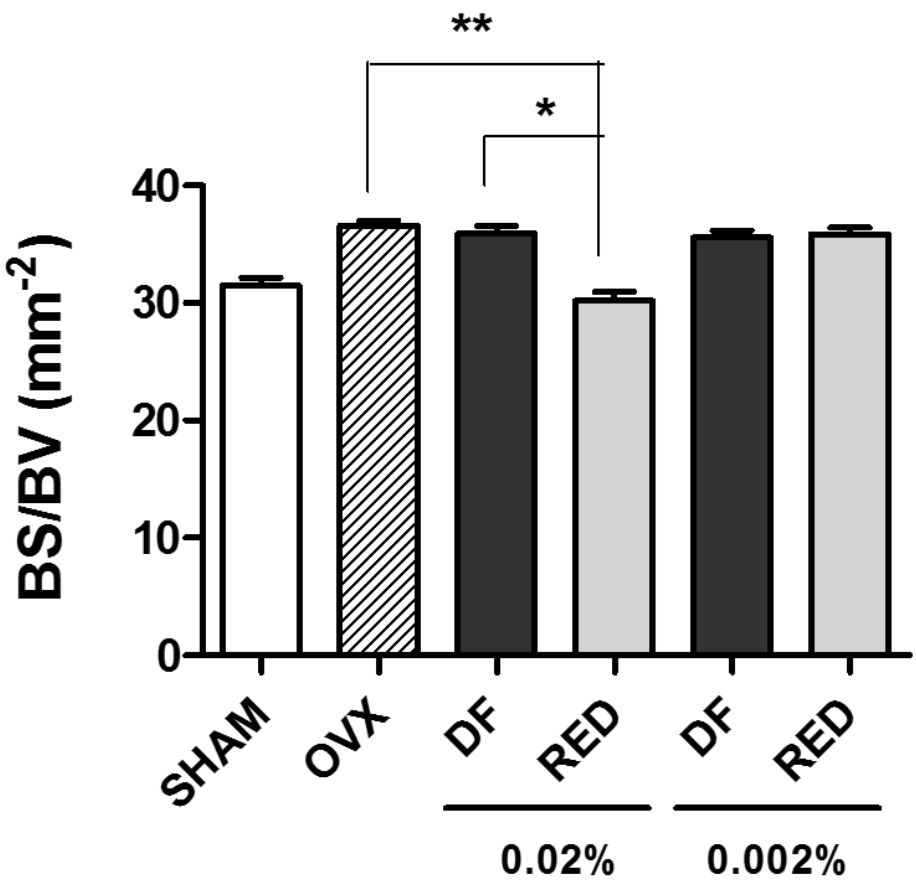

Fig. 2-22. Effect of RIS administration using the RED patch on ovariectomized mouse bone. Bone surface (BS) /BV in vertebras of the ovariectomized mice. $*P < 0.05$, $**P < 0.005$.

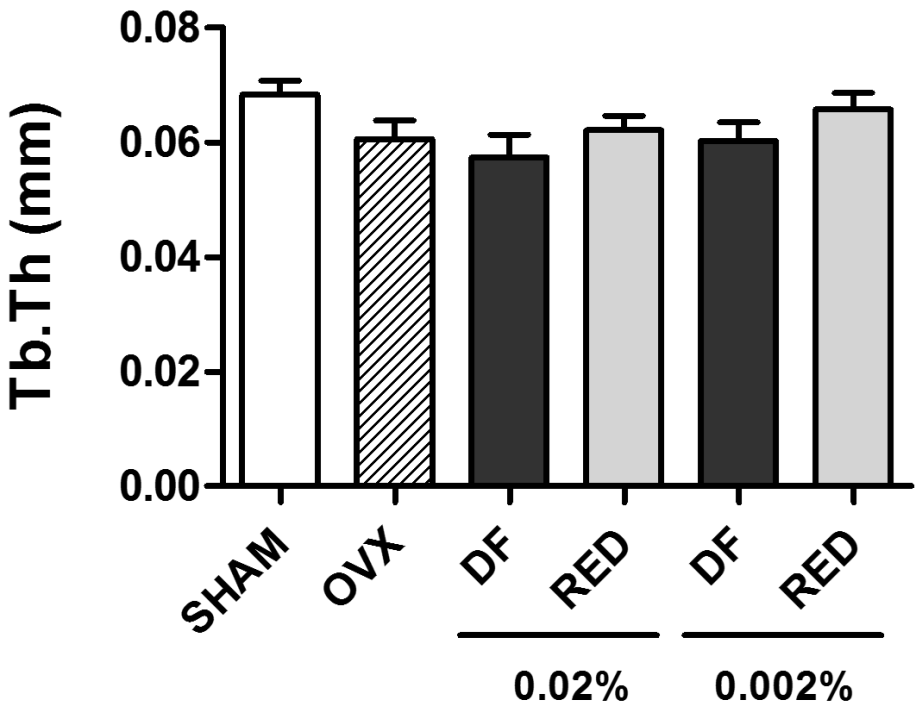

Fig. 2-23. Effect of RIS administration using the RED patch on ovariectomized mouse bone. Trabecular thickness (Tb.Th) in vertebras of the ovariectomized mice.

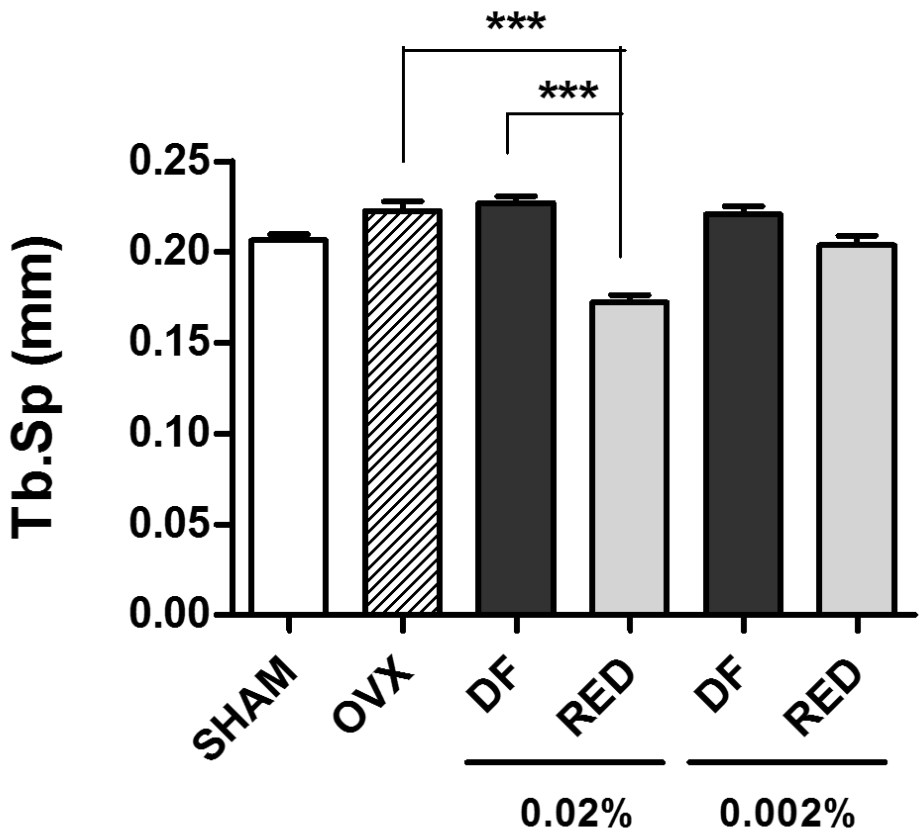

Fig. 2-24. Effect of RIS administration using the RED patch on ovariectomized mouse bone. Trabecular separation (Tb.Sp) in vertebras of the ovariectomized mice. ***$P < 0.0005$.

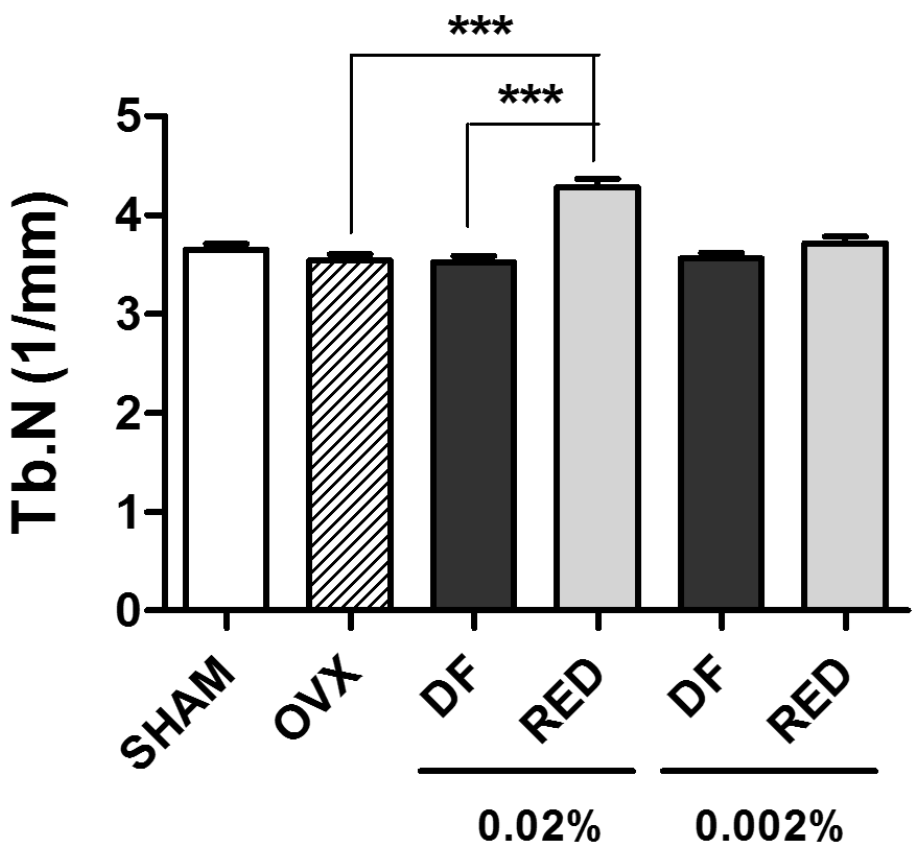

Fig. 2-25. Effect of RIS administration using RED on ovariectomized mouse bone. Trabecular number (Tb.N) in vertebras of the ovariectomized mice. ***$P < 0.0005$.

2.4. Conclusions

In this study, we present a new transdermal drug delivery system based on a miniaturized and disposable patch-type RED. *In vitro* study revealed that the penetration rate of all the model drugs by means of the RED patch significantly increased compared with the DF administration while residual drugs in the skin remained much lower than the penetrated amounts. Especially, although the RIS delivery based on passive diffusion insufficiently penetrates the skin owing to hydrophilic and negatively charged characteristic, the remarkably enhanced delivery rate was observed (~36-fold higher than the DF delivery). Then, as an example of clinical application, osteoporosis-induced mice were treated with 0.02% RIS by means of the RED patches and much cured after 30 days from the day of the ovary removal (1 h administration every 10 days for 30 days) compared with only diffusively administrated mice. Our previous report demonstrated that accumulative and topical administration of RIS (0.02% in PBS, 3 times a week, total 15 times by passive diffusion showed high therapeutic effects. [13] However, the RIS delivery with the RED patch in this study exhibited the excellent

curative effects despite of much less dose numbers with the short administration time (1 h administration, total 3 times for 30 days).

The RED patch-based drug delivery system is somewhat analogous to the conventional iontophoresis in terms of delivering principle which exploits ionic flows generated from external power source. The RED patch does not involve any metal electrodes while conventional iontophoretic device requires noble metal electrodes (Pt and Ag) to convert electronic current from power source to ionic current for the delivery of charged drugs. There are some critical issues originating from the use of metal electrodes. In the case of Pt, electrochemical reactions lead to power loss because of the necessary potential for the water splitting (i.e. 1.29 V at least). [14, 15] Drug dissociations and a pH change will also be induced by the electrochemical reactions. In the case of Ag that is the most efficient material for iontophoresis, it is not suitable for the purpose of long-term drug delivery. [16, 17] The electrochemical reactions at silver anode build up silver chloride with simultaneous depletion of silver while silver chloride cathode generates chloride ions. The competing charge carriers (e.g. H^+ by Pt and Cl^- from Ag/AgCl) which possess

higher mobility than the drugs are inevitably produced, leading to decreased delivery efficiency with time of administration. Our comparison study of the RED system with and without electrodes clearly verified the competing charge effects (Cl^- with RIS) on the efficacy of drug delivery. Therefore, the RED patch in this study greatly eliminates various side effects coming from the electrochemical reactions while increasing the efficacy of drug delivery.

Although the RED patch successfully enhanced the penetration rate of drugs through mouse skin, the device requires further improvements for the purpose of human therapy in terms of the size of the RED patch and the range of safe and acceptable current density to the skin. The size of the RED patch would be optimized for the attachment of human skin, e.g. scale of plane area or thinner configurations to offer flexible and comfort wearability during the administration. The initial voltage of the RED to control current amplitude also needs optimization process for the human skin because resistance of human skin differs from that of mouse skin. Safe and tolerated current density are of importance for conventional

iontophoretic drug delivery due to the risk of skin irritations and burns arisen from the pH change. [5] However, the RED patch system in this study does not involve any electrochemical reactions (faradaic reactions), implying that the range of tolerated current density as well as efficacy of drug delivery rate would be enhanced. The disposable RED patch-based transdermal drug delivery system can be applied to the various drugs, for example, any small molecules even up to a few thousand Daltons. Considering many advantages of the RED patch, e.g. no toxicity, simple fabrication with low expense, and feasibility to the various drugs, the new transdermal drug delivery system using the RED patch is a promising *modus operandi* to deliver therapeutic agents and can serve as an alternative way to the current delivery techniques.

2.5. References

[1] M. R. Prausnitz, S. Mitragotri and R. Langer, *Nature reviews Drug discovery*, 2004, **3**, 115–124.

[2] M. R. Prausnitz and R. Langer, *Nat Biotech*, 2008, **26**, 1261–1268.

[3] R. M. T. Tanner, *Skin Research and Technology*, 2008, **14**, 249–260.

[4] Y. N. Kalia, V. Merino and R. H. Guy, *Dermatologic clinics*, 1998, **16**, 289–299.

[5] Y. N. Kalia, A. Naik, J. Garrison and R. H. Guy, *Advanced drug delivery reviews*, 2004, **56**, 619–658.

[6] P. D ł ugo ł ęcki, A. Gambier, K. Nijmeijer and M. Wessling, *Environmental science & technology*, 2009, **43**, 6888–6894.

[7] J. Veerman, M. Saakes, S. Metz and G. Harmsen, *Journal of Membrane Science*, 2009, **327**, 136–144.

[8] N. Y. Yip, D. A. Vermaas, K. Nijmeijer and M. Elimelech, *Environmental science & technology*, 2014, **48**, 4925–4936.

[9] R. E. Pattle, *Nature*, 1954, **174**, 660.

[10] B. Abrahamsen, *Calcified tissue international*, 2010, **86**, 421–435.

[11] A. Choi, H. Gang, J. Whang and H. Gwak, *Drug Delivery*, 2010, **17**, 249-254.

[12] J. K. Brooks, A. J. Gilson, A. J. Sindler, S. G. Ashman, K. G. Schwartz and N. G. Nikitakis, *Oral Surgery, Oral Medicine, Oral Pathology, Oral Radiology, and Endodontology*, 2007, **103**, 780-786.

[13] S. H. Nam, J.-H. Jeong, X. Che, K.-E. Lim, H. Nam, J.-S. Park and J.-Y. Choi, *Bone*, 2012, **50**, 149-155.

[14] P. Singh and H. I. Maibach, *Critical reviews in therapeutic drug carrier systems*, 1993, **11**, 161-213.

[15] P. Batheja, R. Thakur and B. Michniak, *Expert Opin Drug Deliv*, 2006, **3**, 127-138.

[16] V. Merino, A. López, Y. N. Kalia and R. H. Guy, *Pharmaceutical research*, 1999, **16**, 758-761.

[17] J. D. Byrne, M. N. Jajja, A. T. O' Neill, L. R. Bickford, A. W. Keeler, N. Hyder, K. Wagner, A. Deal, R. E. Little and R. A. Moffitt, *Science translational medicine*, 2015, **7**, 273ra214-273ra214.

[18] s. H. Nam, Y. J. Xu, H. Nam, G.-w. Jin, Y. Jeong, S. An and J.-S. Park, *International journal of pharmaceutics*, 2011, **419**, 114-120.

[19] G. Bhatia and A. K. Banga, *BioMed research international*, 2014, **2014**.

[20] T. Gratieri, E. Pujol-Bello, G. M. Gelfuso, J. G. de Souza, R. F. Lopez and Y. N. Kalia, *European Journal of Pharmaceutics and Biopharmaceutics*, 2014, **86**, 219-226.

국문초록

Part 1: Label-Free Detection of Biomarkers in Human Serum

무표지(label-free) 검출 방법은 바이오마커를 신속하고도 간편하게 검출할 수 있다는 큰 장점을 제공한다. 하지만 센서 표면에 목표 분자가 아닌 다른 분자들에 의한 비특이적 흡착도 센서의 신호에 영향을 주게 된다. 따라서 혈액과 같은 복잡한 생체 시료에서는 비특이적 흡착 현상이 센서의 정확도뿐만 아니라 재현성도 떨어뜨리므로 질병의 진단과 진행 정도의 정확한 정보를 제공하기가 더욱 더 어렵게 된다. 본 연구에서는 금 박막으로 둘러싸인 자성 마이크로 입자에 자가조립단층(self-assembled monolayer, SAM)을 도입하여 혈액 시료에서 비특이적 흡착을 효과적으로 방지하고자 하였다. 비특이적 흡착을 효과적으로 방지하는 것으로 잘 알려져 있는 oligo ethylene glycol 체인과 혈액 바이오마커 검출을 위한 항체를 고정시킬 수 있는 carboxy 그룹이 존재하는 유기 연결 분자를 SAM 형성을 위해 금 박막에 도입하였다. 이 특정 항체가 고정되어 있는 금 박막 자성입자를 혈액에 노출시켜 원하는 목표 물질만 선택적으로 농축, 분리한 후 MALDI-TOF MS 분석을 통해 정량하였다. 금 박막 자성입자의 비특이적 흡착

방지 효과의 정도를 알아보기 위해 단백질의 분리, 농축의 목적으로 시중에 판매되고 있는 마이크로 입자들과 체계적으로 비교, 분석하였다. 그 결과, 우리가 사용한 금 박막 자성입자가 비특이적 흡착을 방지함과 동시에 목표 분자를 가장 효과적으로 분리, 농축시키는 능력이 있음을 확인하였다. 또한 급성 심혈관계 질환과 관련 있는 myoglobin 바이오마커를 이용하여 혈청 시료에서도 0.5 ng/mL까지 검출할 수 있음을 확인하였으며 자성 입자를 사용하여 바이오마커를 검출한 보고된 논문 결과들과 비교하여 더 뛰어난 신호 검출 한계를 보여주었다. 최종적으로, MALDI-TOF MS가 제공하는 무표지 검출 및 신속 분석의 장점과 금 박막 자성입자가 가지는 효과적인 비특이적 흡착 방지 장점을 결합하여 혈청에서 3개의 다른 바이오마커를 동시에 분석하는 다중 검출도 가능함을 증명하였다.

Part 2: A New Drug Delivery System Based on Reverse Electro-dialysis

역전기투석(RED)은 태양에너지와 달리 안정적이고 지속적인 전력 생산이 가능한 점, 친환경 무한정 자원인 강물과 바닷물을 이용하는 장점 등으로 새로운 친환경 전력생산시스템으로서 유럽을 중심으로 큰 주목을 받아 왔다. 하지만 이온교환막의 고비용, biofouling으로 인한

내구성 감소, 낮은 전력생산 밀도로 인해 RED 기반 발전시스템의 대형화 및 산업화는 초기단계에 머물러 있다. 본 연구에서는 RED의 본래 목적인 대형 전력 생산이 아니라 친환경 에너지원, 저전력 생산 밀도의 특징을 활용하여 적용될 수 있는 하나의 예로서, 피부를 통해 약물을 전달하는 새로운 경피 약물 전달시스템(transdermal drug delivery system)을 개발하였다. 기존 약물의 확산에만 의존하는 경피 전달은 피부의 각질층이 매우 큰 장벽으로 작용하여 약물이 피부를 통과하는데 긴 시간이 소요되며 전달되는 양도 작다. 이를 해결하기 위해 19세기 초에 제시된 방법이 이온토포레시스(iontophoresis)이며, 두 개의 전극으로부터 생성된 전기장에 의해 약물이 피부를 지나 신체 내부로 신속하게 투입되는 방법이다. 하지만 이온토포레시스는 피부에 부착된 전극 표면에서 발생하는 전기화학의 결과로 화학적 화상을 유발하거나 약물이 분해되는 위험, 수소 및 염소 이온으로 인한 약물 전달 효율의 감소의 여러 가지 단점이 있다.

본 연구에서는 피부에 부착되는 전극 없이 약물을 전달할 수 있는 새로운 경피 약물 전달 시스템을 고안하였다. In vitro 쥐 피부 실험을 통해 단지 확산에 의존하여 약물을 전달하는 방법에 비해 RED를 이용한 약물 전달 방법이 20배 가량 약물 전달량을 증가시키는 것을 확인하였다. 또한 골다공증이 유발된 쥐에 risedronate 약물을 RED를

통해 주입하여 실제로 골다공증 예방 및 치료에 큰 효과가 있는 것도 증명하였다.

키워드: 금 표면, 비특이적 흡착, 질량분석법, 역전기투석, 경피약물전달, 골다공증

Student Number: 2011-30098